Monthly Notices
of the
ROYAL ASTRONOMICAL SOCIETY

MNRAS **492,** 5592–5606 (2020)
Advance Access publication 2020 January 20

doi:10.1093/mnras/staa157

The high-redshift SFR–M* relation is sensitive to the employed star formation rate and stellar mass indicators: towards addressing the tension between observations and simulations

A. Katsianis [1,2,3★] V Gonzalez,[4,5] D. Barrientos,[3] X. Yang,[1,2] C. D. P. Lagos [6,7,8] J. Schaye [9] P. Camps,[10] A. Trčka [10] M. Baes [10] M. Stalevski [10,11] G. A. Blanc[3,12] and T. Theuns[13]

[1]*Tsung-Dao Lee Institute, Shanghai Jiao Tong University, Shanghai 200240, China*
[2]*Department of Astronomy, Shanghai Key Laboratory for Particle Physics and Cosmology, Shanghai Jiao Tong University, Shanghai 200240, China*
[3]*Department of Astronomy, Universitad de Chile, Camino El Observatorio 1515, Las Condes, Santiago, Chile*
[4]*Chinese Academy of Sciences South America Center for Astronomy, China-Chile Joint Center for Astronomy, Camino del Observatorio 1515, Las Condes, Chile*
[5]*Centro de Astrofísica y Tecnologías Afines (CATA), Camino del Observatorio 1515, Las Condes, Santiago, Chile*
[6]*International Centre for Radio Astronomy Research (ICRAR), M468, University of Western Australia, 35 Stirling Hwy, Crawley, WA 6009, Australia*
[7]*ARC Centre of Excellence for All Sky Astrophysics in 3 Dimensions (ASTRO 3D), 44 Rosehill street Redfern, NSW 2016, Australia*
[8]*Cosmic Dawn Center (DAWN), University of Copenhagen, Vibenshuten, Lyngbyvej, 2 DK - 2100 Copenhagen, Denmark*
[9]*Leiden Observatory, Leiden University, PO Box 9513, Leiden NL-230 0 RA, the Netherlands*
[10]*Sterrenkundig Observatorium, Universiteit Gent, Krijgslaan 281, Gent B-9000, Belgium*
[11]*Astronomical Observatory, Volgina 7, Belgrade 11060, Serbia*
[12]*Observatories of the Carnegie Institution for Science, 813 Santa Barbara St, Pasadena, CA 91101, USA*
[13]*Department of Physics, Institute for Computational Cosmology, University of Durham, South Road, Durham DH1 3LE, UK*

Accepted 2019 December 24. Received 2019 November 23; in original form 2019 July 23

ABSTRACT

There is a severe tension between the observed star formation rate (SFR)–stellar mass ($M_\star$) relations reported by different authors at $z = 1$–4. In addition, the observations have not been successfully reproduced by state-of-the-art cosmological simulations that tend to predict a factor of 2–4 smaller SFRs at a fixed $M_\star$. We examine the evolution of the SFR–$M_\star$ relation of $z = 1$–4 galaxies using the SKIRT simulated spectral energy distributions of galaxies sampled from the Evolution and Assembly of GaLaxies and their Environments simulations. We derive SFRs and stellar masses by mimicking different observational techniques. We find that the tension between observed and simulated SFR–$M_\star$ relations is largely alleviated if similar methods are used to infer the galaxy properties. We find that relations relying on infrared wavelengths (e.g. 24 μm, MIPS – 24, 70, and 160 μm or SPIRE – 250, 350, and 500 μm) have SFRs that exceed the intrinsic relation by 0.5 dex. Relations that rely on the spectral energy distribution fitting technique underpredict the SFRs at a fixed stellar mass by −0.5 dex at $z \sim 4$ but overpredict the measurements by 0.3 dex at $z \sim 1$. Relations relying on dust-corrected rest-frame ultraviolet luminosities, are flatter since they overpredict/underpredict SFRs for low/high star-forming objects and yield deviations from the intrinsic relation from 0.10 to −0.13 dex at $z \sim 4$. We suggest that the severe tension between different observational studies can be broadly explained by the fact that different groups employ different techniques to infer their SFRs.

Key words: galaxies: evolution – galaxies: star formation.

1 INTRODUCTION

Star formation rate (SFR) and stellar mass ($M_\star$) are two fundamental properties of galaxies since each can provide a useful census for galaxy formation and evolution. The SFR–$M_\star$ plane can be loosely

★ E-mail: kata@sjtu.edu.cn

separated into three different Gaussian distributions (Bisigello et al. 2018), corresponding to (1) the quenched/passive galaxies, (2) the star-forming galaxies, and (3) the starburst galaxies. A range of observational studies has exhibited the existence of a relation between SFR and stellar mass ($M_\star$) for $z \simeq 0$–8, especially for the star-forming population (Noeske et al. 2007; Elbaz et al. 2011; Whitaker et al. 2014; Tomczak et al. 2016; Davies et al. 2019; Katsianis et al. 2019; Popesso et al. 2019), to the extent that such correlation has been labelled as the main sequence (MS).[1] Samples with no selection of star-forming galaxies produce either flatter or 'bending' SFR–$M_\star$ relations at low redshifts ($z < 1$) and higher masses (Drory & Alvarez 2008; Bauer et al. 2011; Bisigello et al. 2018) due to the presence of the quenched population, which contains galaxies with lower SFRs at a fixed stellar mass.

In order to retrieve the intrinsic properties of galaxies and determine the SFR–$M_\star$ relation, different observational studies rely on different models and SFR/$M_\star$ diagnostics. Stellar masses are typically calculated via the spectral energy distribution (SED) fitting technique (e.g. Kriek et al. 2009; Conroy 2013; Boquien et al. 2019), for which various assumptions are required (e.g. initial mass function, star formation history, dust attenuation model, and metallicity fraction). Furthermore, different studies employ different calibrations/wavelengths in order to derive galaxy SFRs such as infrared $(IR)_{24\,\mu m}$ luminosities (Rodighiero et al. 2010; Guo, Zheng & Fu 2013; Whitaker et al. 2014; Guo et al. 2015), Hα luminosities (Sánchez et al. 2018; Cano-Díaz et al. 2019), the SED fitting technique (Drory & Alvarez 2008; Kajisawa et al. 2010; Bauer et al. 2011; Karim et al. 2011; de Barros, Schaerer & Stark 2014; Kurczynski et al. 2016) or ultraviolet (UV) luminosities (Salim et al. 2007; Bouwens et al. 2012; Santini et al. 2017; Blanc et al. 2019). A number of questions arise. The different diagnostics, assumptions, and methodologies used by different observational studies produce results that are in agreement? If not, is there a way to decipher the effect of the assumed methodology?

In the last years, an increasing number of authors have reported a discrepancy between the SFRs inferred by different methodologies (Boquien, Buat & Perret 2014; Fumagalli et al. 2014; Hayward et al. 2014; Utomo et al. 2014; Davies et al. 2016, 2017; Katsianis et al. 2017b). In addition, Katsianis, Tescari & Wyithe (2016) demonstrated that there is a severe tension of $\simeq 0.2-1$ dex between the observed SFR–$M_\star$ relations at $z \sim 1$–4 reported by different groups and suggested that the lack of consensus between different authors has its roots in the diversity of techniques used in the literature to estimate SFRs and also in sample selection effects. Furthermore, Davies et al. (2016) pointed out that different methods yield relations with inconsistent slopes and normalizations. In addition, Speagle et al. (2014) and Renzini & Peng (2015) suggested that the logarithmic slope α of the MS relation, which can be fitted by $\mathrm{Log_{10}(SFR)} = \alpha \mathrm{Log_{10}M_\star} + \mathrm{c}$, ranges from ~ 0.4 up to ~ 1.0 from study to study, while the normalization c differs from -8.30 up to -1.80 at redshift $z \sim 2.0$. Some authors find significant evolution for the slope ($\alpha(z) = 0.70$–$0.13z$) at $z \sim 0$–2.5 (Whitaker et al. 2012), while others indicate no evolution (Dunne et al. 2009; Karim et al. 2011). The scatter of the relation also varies in the literature. Some authors report that σ_{SFR} is constant with stellar mass and redshift (Rodighiero et al. 2010; Schreiber et al. 2015), while others suggest that the dispersion is mass/redshift dependent (Guo et al. 2013; Katsianis et al. 2019).

Cosmological hydrodynamic simulations from different collaborations such as Evolution and Assembly of GaLaxies and their Environments (EAGLE; Crain et al. 2015; Schaye et al. 2015), Illustris (Vogelsberger et al. 2014), IllustrisTNG (Pillepich et al. 2018), and ANGUS (Tescari et al. 2014; Katsianis, Tescari & Wyithe 2015), have successefully replicated a range of observables and thus can provide information about the SFR–$M_\star$ relation. However, the simulations have not been able to reproduce most of the observed SFR–$M_\star$ relations reported in the literature. Indeed, most groups report tension with observations, especially at $z \simeq 1$–2 (Furlong et al. 2015; Sparre et al. 2015; Katsianis et al. 2016; Donnari et al. 2019). The questions that arise are why cosmological hydrodynamic simulations have been unable to reproduce most of the observed SFR–$M_\star$ relations at high redshifts? Can they provide insights on the tension between different observational studies?

Evaluating the determination of galaxy properties from different methodologies requires a galaxy sample with known intrinsic properties. Thus, a range of articles has examined separately the recovery of stellar masses (Wuyts et al. 2009; Hayward & Smith 2015; Torrey et al. 2015; Camps et al. 2016; Price et al. 2017) and SFRs (Kitzbichler & White 2007; Maraston et al. 2010; Pforr, Maraston & Tonini 2012) using mock/simulated galaxies. Hence, mock surveys (Snyder et al. 2011; Camps et al. 2018; Liang et al. 2019), which involve objects with known SFRs, stellar masses, and fluxes at various key bands (e.g. *GALEX*–FUV, SDSS-u, 2MASS-Ks, WISE 3.4 μm or *Spitzer* 24 μm), are ideal to explore the effect of SFR and $M_\star$ diagnostics on the inferkatsianis antoniosred SFR–$M_\star$ relation.

In this paper, we employ the mock SEDs described in Camps et al. (2018) and derive properties following observational methodologies used in the literature. We derive stellar masses through the SED fitting technique (Kriek et al. 2009). SFRs are calculated using the 24, 70, and 160 μm luminosities and their relation with the total IR (TIR) luminosity (Dale & Helou 2002; Wuyts et al. 2008), fitting the SPIRE 250, 350, and 500 μm fluxes to the Dale et al. (2014) templates, dust-corrected UV luminosities via the infrared excess (IRX)–β relation (Meurer, Heckman & Calzetti 1999), and the SED fitting technique. The analysis allows us to address the discrepancy between different observational methodologies to infer SFRs and stellar masses while it provides insights on the tension between cosmological hydrodynamic simulations and observational studies at high redshifts. In Section 2, we present a comparison between a range of observed relations and EAGLE simulations. In Section 3, we briefly present the EAGLE + SKIRT data, while in Section 3.1 we describe the methodologies used to derive SFRs and stellar masses from the simulated galaxies. In Section 4, we perform the comparison between observations and simulations. In Section 5, we draw our conclusions. In Appendix A, we provide a comparison between the inferred and intrinsic SFRs and stellar masses.

2 THE COMPARISON BETWEEN OBSERVED AND SIMULATED SFR–$M_\star$ RELATIONS

2.1 EAGLE versus observations

The EAGLE simulations (Crain et al. 2015; Schaye et al. 2015; McAlpine et al. 2016) are a well-studied suite of cosmological

[1] In order to select star-forming galaxies and define the MS, different authors use different criteria (e.g. minimum threshold for of sSFR = SFR/$M_\star$, UVJ colour–colour selection, ridge line in the 3D surface defined by the SFR–mass–number density relation), which should ideally remove galaxies with low sSFRs from their 'parent' samples. However, the thresholds differ significantly in value from one study to another (Renzini & Peng 2015) making the comparison between the results of different authors challenging.

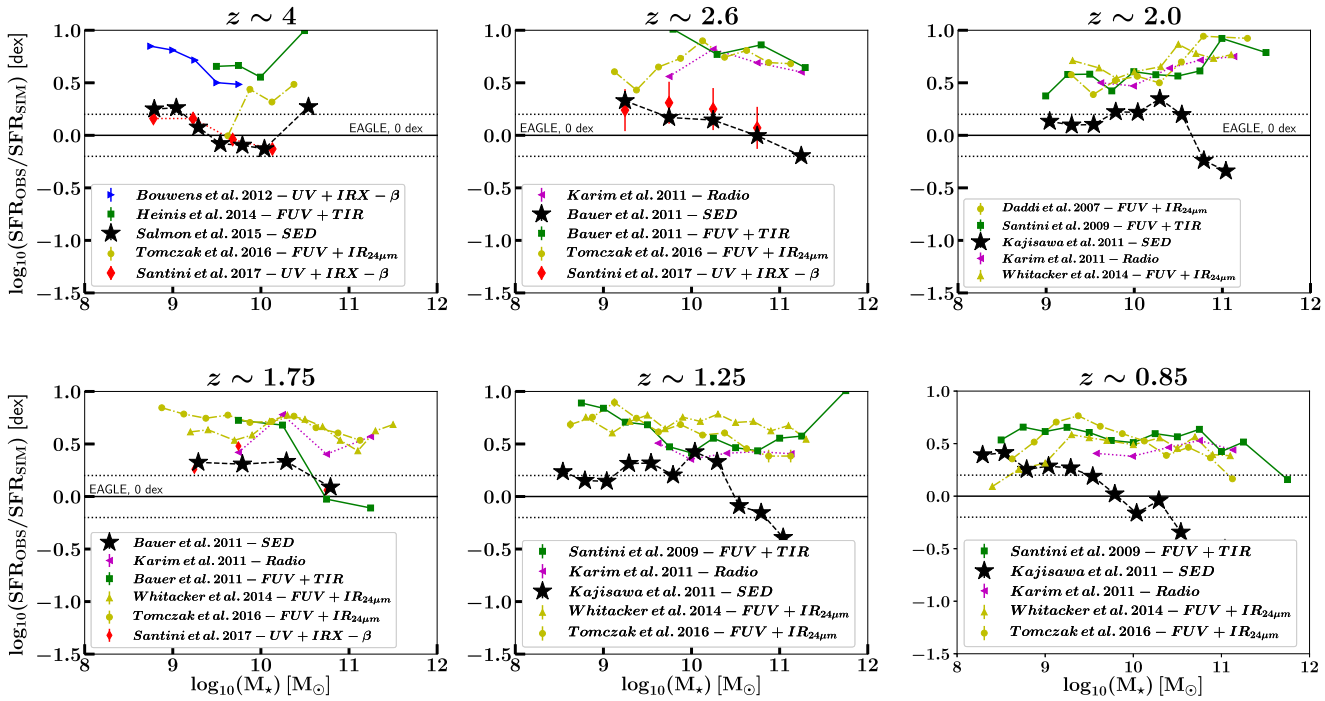

Figure 1. The offset, in dex, between a range of observations with respect the SFR−$M_\star$ relation from the EAGLE simulation reference model with different panels showing different redshifts, ranging from $z \simeq 0.85$ to 4. The 0 dex line represents the EAGLE reference model. The observed stellar masses when necessary were altered into the Chabrier (2003) IMF and the conversion laws between luminosities and observed SFRs were updated to the Kennicutt & Evans (2012) relations. Top left-hand panel: The blue right-pointing triangles represent the observations of Bouwens et al. (2015; UV + IRX–β), the green squares Heinis et al. (2014; FUV + TIR), the black stars the observations of Salmon et al. (2015; SED fitting), the orange circles Tomczak et al. (2016; FUV + IR), and the red diamonds the results from Santini et al. (2017; UV + IRX–β). Middle top Panel: The Magenta left-pointing triangles represent the results from Karim et al. (2011; Radio), the black stars Bauer et al. (2011; SED fitting), the dark green squares Bauer et al. (2011; FUV + TIR), the orange triangles represent Whitaker et al. (2014) and Tomczak et al. (2016; FUV + IR). Top right-hand panel: The yellow circles represent the results from Daddi et al. (2009). Note that other observational studies present in this panel are described in the previous panels. Middle bottom Panel: The green squares represent the results from Santini et al. (2009; FUV + TIR), the black stars the observations from Kajisawa et al. (2010; SED fitting). Observational studies report results that can differ by 0.2–1.2 dex. The EAGLE reference model is usually more consistent with the results reported by authors who used SED fitting (the black stars) to derive both SFRs and stellar masses (Katsianis et al. 2016) but the offset, even from these observations can be up to 0.4 dex.

hydrodynamical simulations with the reference model being able to produce galaxies with realistic SFRs and stellar masses. It broadly reproduces the observed SFR function of $z = 0$–8 galaxies (Katsianis et al. 2017b), the evolution of the stellar mass function (Furlong et al. 2015), and the scatter of the sSFR–$M_\star$ relation (Davies et al. 2019; Katsianis et al. 2019; Matthee & Schaye 2019) at $z \simeq 0$–4. The reference simulation spans a 100 co-moving Mpc per side in a cubic, periodic volume. The initial conditions were generated using the IC_2LPT_GEN code (Jenkins 2010). EAGLE–REF tracks the evolution of baryonic gas, stars, non-baryonic dark matter particles, and massive black holes from $z = 127$ to $z = 0$. It includes various physical prescriptions such as SNe feedback (Dalla Vecchia & Schaye 2012; Katsianis et al. 2017b), active galactic nuclei (AGN) feedback (Springel, Di Matteo & Hernquist 2005; Rosas-Guevara et al. 2016), metal cooling (Wiersma et al. 2009), and star formation (Schaye & Dalla Vecchia 2008) assuming a Chabrier (2003) initial mass function (IMF). It follows 2×1504^3 particles with an equal number of gas and dark matter elements with initial mass of dark matter particles $m_\mathrm{D} = 9.7 \times 10^6\,\mathrm{M_\odot}$ and particle gas mass of $m_\mathrm{g} = 1.8 \times 10^6\,\mathrm{M_\odot}$. The reference simulation produce the observed molecular hydrogen abundances (Lagos et al. 2015), supermassive black holes evolution (Rosas-Guevara et al. 2016), angular momentum evolution (Lagos et al. 2017), and quenching histories of cluster galaxies (Pallero et al. 2019). However, the simulation is unable to reproduce the observed SFR–$M_\star$ relation especially at $z \simeq 1$–2 (Furlong et al. 2015). Katsianis et al. (2016), demonstrated that the EAGLE, Illustris, and ANGUS simulations alongside with semi-analytic models (Dutton, van den Bosch & Dekel 2010) produce almost identical relationships, indicating that the tension of simulations with observations is a common finding between different collaborations. The discrepancy between observed and simulated relations is typically −0.2–0.8 dex, depending on mass, redshift, sample selection method, and observational technique used to derive SFRs and stellar masses, with the simulations predicting a factor of 2–4 smaller SFRs at a fixed $M_\star$ than observed.

In Fig. 1, we present the offset of a range of observations with respect to the EAGLE reference model (represented by the black 0 dex line). In the top left-hand panel ($z \simeq 4.0$), the blue triangles represent the observations of Bouwens et al. (2012; UV + IRX–β), the green squares Heinis et al. (2014; FUV + TIR), the black stars the observations of Salmon et al. (2015; SED fitting), the orange circles Tomczak et al. (2016; FUV + IR), and the red diamonds the results from Santini et al. (2017; UV + IRX–β). We note that in order to perform a consistent and up to date comparison between observational studies and EAGLE, the observed stellar masses when necessary were altered into the Chabrier (2003) IMF and the conversion laws between luminosities and observed SFRs

were updated to the Kennicutt & Evans (2012) relations. We also note that the observed relations and the comparison between them does not change significantly after the above calibrations (Katsianis et al. 2016). We can see that the observations of Heinis et al. (2014) and Bouwens et al. (2012) differ from the EAGLE reference model by $\simeq$0.5−1 dex. However, the Salmon et al. (2015) and Santini et al. (2017) observations are within $\simeq$0–0.3 dex from the predictions. This behaviour is found at all redshifts with the reference EAGLE model and observations having offset SFRs from −0.2 to 1.0 dex depending on masses and redshifts. However, we note that there is a similar tension between the observed SFR–$M_\star$ relation reported by different authors. For example, Heinis et al. (2014) and Salmon et al. (2015) results differ by 0.6–0.8 dex at $z \simeq 4$. Different authors use different diagnostics, assumptions, and wavelengths to infer galaxy SFRs. Thus, it is interesting to derive SFR–$M_\star$ relations using a set of artificial/simulated galaxies for which we have access to their SFRs, stellar masses, and full SEDs. We can then mimic the methodologies used by different observational studies and explore further the inconsistency between hydrodynamic simulations and observations and the discrepancy between the results reported by a range groups.

We have to note that selection effects, besides the criteria used to define MS objects (Renzini & Peng 2015), can also affect any comparison between observational studies (Speagle et al. 2014) and can enhance the disagreement with simulations (Katsianis et al. 2016). Some 'parent' selection methods commonly used in the literature include the B–z versus z–K (sBzK) technique (Daddi et al. 2004, 2007; Kashino et al. 2013), the Lyman break technique (Bouwens et al. 2012), and cuts on the colour–magnitude diagram (Elbaz et al. 2007). The above methods pre-select star-forming galaxies and steeper slopes are expected for the derived SFR–$M_\star$, since a large portion of less active galaxies that would be classified as star-forming is prematurely excluded.[2] We choose to neglect the effect of parent sample selection in our comparisons with simulations, following previous studies (Furlong et al. 2015; Sparre et al. 2015). Complicating further our analysis by reckoning numerous sample selection criteria that are greatly different from study to study would divert our focus from the main goal of our work, which is to investigate the impact of the employed methodology to derive galaxy properties using mock galaxies on the SFR–$M_\star$ relation.

3 THE EAGLE + SKIRT DATA

Camps et al. (2018) performed full 3D radiative transfer post-processing simulations applying the SKIRT code (Baes et al. 2003, 2011; Camps & Baes 2015) on the EAGLE galaxies. The authors calculated mock observables that fully took into account the absorption, scattering, and thermal emission from the EAGLE simulation. Next, we briefly describe the procedure.

For each stellar particle, an SED was assigned that was acquired from the GALEXEV library (Bruzual & Charlot 2003), based on the mass of the particle, age, and metallicity. For each star-forming particle, an SED was acquired from the MAPPINGS III templates (Groves et al. 2008) based on its SFR, pressure of the interstellar medium, compactness, covering fraction of the photodissociation region and metallicity. MAPPINGS models are used to describe the dusty H II regions. The dust distribution is obtained from the distribution of gas while the assumed model is Zubko, Dwek & Arendt (2004). The dust mass is derived from the cool and star-forming gas, and correlates with the fraction of metals in dust ($f_{\rm dust}$). The adopted values for the covering fraction, the dust-to-metal ratio and $f_{\rm dust}$ are based on the following scaling relations: (1) the sub-mm colour diagram, (2) the specific dust mass ratio versus stellar mass, and (3) the NUV–r colour relation. The calibration was done between galaxies from the *Herschel* Reference Survey (HRS; Boselli et al. 2010; Cortese et al. 2012) and a matched sub-sample of 300 EAGLE galaxies (Camps et al. 2016). The adopted value of covering fraction is $f_{\rm PDR} = 0.1$. The metal fraction is set to be $f_{\rm dust} = 0.3$ (Brinchmann et al. 2013). The dust density distribution of the system is discretized over an octree grid (Saftly et al. 2013). Physical quantities, such as the radiation field and dust density, are assumed to be constant. The smallest possible cell is 60 pc on a side. In order to perform the radiative transfer simulation, it is important to have a sufficiently resolved dust distribution. Thus, the EAGLE + SKIRT sample excludes galaxies with low SFRs that have little or no dust (Camps et al. 2018).[3]

The input SEDs and dust properties are sampled on a single wavelength grid that performs the radiative transfer calculations. Photon packages are given wavelengths that correspond to the grid points, dust absorption, and re-emission. The output fluxes are recorded on the same grid that has 450 wavelenght points from 0.02 to 2000 μm on a logarithmic scale. The band-integrated fluxes and absolute magnitudes that were produced correspond to the following filters: GALEX FUV/NUV (Morrissey et al. 2007), $\rm SDSS_{\it ugriz}$ (Doi et al. 2010), 2MASS JHK (Cohen, Wheaton & Megeath 2003), WISE W1/W2/W3/W4 (Wright et al. 2010), *Spitzer* MIPS 24/70/160 (Rieke et al. 2004), *Herschel* PACS 70/100/160 (Poglitsch et al. 2010), and *Herschel* SPIRE 250/350/500 (Griffin et al. 2010). To obtain the integrated fluxes, the simulated SEDs were convolted with the instrument's response curve. The procedure depends on whether the instrument counts photons or measures energy (bolometers) and is summarized in detail at the appendix A of Camps et al. (2016). To obtain broad-band magnitudes in the rest frame, the detected SEDs are convolted with the corresponding response curves while the resulting fluxes are converted to absolute AB magnitudes, taking into account the fixed assumed galaxy-detector distance of 20 Mpc (the median distance of the HRS sample). To obtain fluxes in the observer frame, the detected SEDs are redshifted and scaled following

$$\mathrm{f_{v,obs}} = (1+z)\left(\frac{20\,\mathrm{Mpc}}{\mathrm{D_L}}\right)^2 \mathrm{f_{v,shifted}}, \quad (1)$$

where z is the galaxy's redshift and $D_{\rm L}$ the corresponding luminosity distance. The $D_{\rm L}$ used are given by Adachi & Kasai (2012) following Baes, Camps & Van De Putte (2017).

Thus, the mock galaxy SEDs consist of UV to sub-mm flux densities and rest-frame luminosities for almost 0.5 million simulated

[2]Speagle et al. (2014) pointed out that the normalization of the MS does not differ significantly between studies that use different parent selection methods. However, the logarithmic slope α differs by ±0.5 from study to study and is typically larger for pre-selected parent star-forming objects. (Oliver et al. 2010; Karim et al. 2011; Sobral et al. 2011; Whitaker et al. 2012; Speagle et al. 2014), well before an MS is defined.

[3]We note that the above pre-selection criteria could exclude some realistic objects but the offset between the SFR–$M_\star$ relations derived from the EAGLE + SKIRT data and the full EAGLE data is small ($\simeq$0.05 dex at $z = 4$, $\simeq$ 0.08 dex at $z = 2$, and $\simeq$ 0.05 dex at $z = 1$). Thus, any comparison between the observed and EAGLE + SKIRT SFR–M⋆ relations at the $\log_{10}(M_\star/\mathrm{M}_\odot)$ $\simeq$ 8.5−11.0 range is not significantly affected by the selection criteria described in Camps et al. (2018).

galaxies, from $z = 0$ to 6. The above data have already been used to investigate the cosmic SED (Baes et al. 2019), the relation between the hosts of merging compact objects to properties of galaxies such as metallicities, SFRs, stellar masses, and colours (Artale et al. 2019), the $\sigma_{\rm sSFR}-{\rm M}_{\star}$ relation (Katsianis et al. 2019), the nature of sub-mm and high-SFR systems (McAlpine et al. 2019), and galaxy number counts at 850 μm (Cowley et al. 2019). We use the same data to study how typical SFR and $\rm M_{\star}$ diagnostics affect the SFR–M⋆ relation and to make a fairer comparison with the observations using the same methods to infer SFRs and stellar masses for the simulated galaxies. We stress that the EAGLE objects that were post-processed by SKIRT were galaxies with stellar masses $\log_{10}(M_{\star}/{\rm M}_{\odot}) > 8.5$, above the resolution limit of 100 gas particles and with sufficient dust content.

3.1 Stellar masses and SFRs from the EAGLE + SKIRT data

To infer stellar masses from the EAGLE + SKIRT galaxies, we use the Fitting and Assessment of Synthetic Templates (FAST) code (Kriek et al. 2009) to fit the mock SEDs, following a similar procedure as various observational studies (González et al. 2012; Botticella et al. 2017; Aird, Coil & Georgakakis 2018). Following the same procedure as in Katsianis et al. (2019), we use the Bruzual & Charlot (2003) stellar population synthesis models and assume an exponentially declining star formation history (SFH) [SFR = exp(−t/tau)] (Fumagalli et al. 2016; Abdurro'uf 2018), the Chabrier IMF (Chabrier 2003), the Calzetti et al. (2000) dust attenuation law (Cullen et al. 2018; McLure et al. 2018b), and a metallicity $\rm Z = 0.2\ Z_{\odot}$ (Chan et al. 2016; McLure et al. 2018a). We note that these assumptions are motivated by observational studies but not necessarily stand neither for the real/observed nor the EAGLE + SKIRT simulated galaxies (in Table 1, we sumarize the SED fitting assumptions used by different authors). We employ numerous wavelengths filters such as $\rm GALEX_{FUV}$, $\rm GALEX_{NUV}$, $\rm SDSS_{\it u}$, $\rm SDSS_{\it g}$, $\rm SDSS_{\it r}$, $\rm SDSS_{\it i}$, $\rm SDSS_{\it z}$, $\rm TwoMass_{\it J}$, $\rm TwoMass_{\it H}$, $\rm TwoMass_{\it Ks}$, $\rm UKIDDS_{\it Z}$, $\rm UKIDDS_{\it Y}$, $\rm UKIDDS_{\it J}$, $\rm UKIDDS_{\it H}$, $\rm UKIDDS_{\it K}$, $\rm Johnson_{\it U}$, $\rm Johnson_{\it B}$, $\rm Johnson_{\it V}$, $\rm Johnson_{\it R}$, $\rm Johnson_{\it I}$, $\rm Johnson_{\it J}$, $\rm Johnson_{\it M}$, $\rm WISE_{\it W1}$, $\rm WISE_{\it W2}$, $\rm WISE_{\it W3}$, $\rm WISE_{\it W4}$, $\rm IRAS_{12}$, $\rm IRAS_{25}$, $\rm IRAS_{60}$, $\rm IRAS_{100}$, $\rm IRAC_{\it I1}$, $\rm IRAC_{\it I2}$, $\rm IRAC_{\it I3}$, $\rm IRAC_{\it I4}$, $\rm MIPS_{24}$, $\rm MIPS_{70}$, $\rm MIPS_{160}$, $\rm PACS_{70}$, $\rm PACS_{100}$, $\rm PACS_{160}$, $\rm SPIRE_{250}$, $\rm SPIRE_{350}$, and $\rm SPIRE_{500}$ in order to limit parameter degeneracies to the SED fitting procedure (Katsianis et al. 2016; Santini et al. 2017).

To derive SFRs from the EAGLE + SKIRT data, we follow a range of techniques:

(1) Employing the SED fitting technique in which the same bands used to derive the stellar masses are exploited (Kriek et al. 2009). We label the above as $\rm SFR_{SED-FAST}$.

(2) Combining the TIR obtained from the 24 μm luminosities and dust-uncorrected FUV (1600 Å). The TIRs are obtained adopting the luminosity-independent conversion from $IR_{24\,\mu{\rm m}}$ (Wuyts et al. 2008) following Franx et al. (2008), Muzzin et al. (2010), Whitaker et al. (2014), and Tomczak et al. (2016). We convert the TIR luminosities and UV luminosities into SFRs following Kennicutt & Evans (2012)[4] while the total SFR is given by

$$\rm SFR_{24\,\mu m} = SFR_{UV-uncor} + SFR_{TIR_{24\,\mu m}}. \quad (2)$$

We label the above as $\rm SFR_{24\,\mu m-Wuyts\,et\,al.\,2008}$.

(3) Combining the TIR luminosities with dust-uncorrected UV emission (1600 Å). The TIR luminosities are estimated from the 24, 70, and 160 μm MIPS luminosities following Verley et al. (2010) and Espada et al. (2019) and employing the relation given by the Dale & Helou (2002) templates[5]. We convert the TIR and dust-uncorrected FUV luminosities into SFRs using Kennicutt & Evans (2012), while the total SFR is obtained from

$$\rm SFR_{24,70,160\,\mu m} = SFR_{UV-uncor} + SFR_{TIR_{24,70,160\,\mu m}}. \quad (3)$$

We label the above as $\rm SFR_{24,70,160\,\mu m-r\,Dale\&Helou\,2002}$.

(4) Using the luminosity emitted by dust derived from the 250, 350, and 500 μm fluxes, the code CIGALE (Boquien et al. 2019) and the Dale et al. (2014) templates combined with the uncorrected FUV light. The dust luminosities and UV luminosities were converted to SFRs using the Kennicutt & Evans (2012) relations. In a similar framework, Heinis et al. (2014) inferred the dust luminosities of the COSMOS galaxies by adjusting the 250, 350, and 500 μm fluxes to the Dale & Helou (2002) templates, using an older version of CIGALE (Noll et al. 2009) and the Kennicutt (1998) relations.[6] The authors combined the above with FUV luminosities (1570−1620 Å) in order to derive the galaxy SFRs. We label the above as $\rm SFR_{250,350,500\,\mu m-C\,Dale\&Helou\,2014}$.

(5) Employing the FUV luminosities (e.g. 1600 Å) dust-corrected using the IRX–β relation (Meurer et al. 1999). In order to obtain the FUV SFRs, we follow the method described in Smit et al. (2012) and Katsianis et al. (2017a). We correct the FUV luminosities assuming the IRX–β relation of Meurer et al. (1999):

$$\rm A_{1600} = 4.43 + 1.99\,\beta, \quad (4)$$

where A_{1600} is the dust absorption at 1600 Å and β is the UV-continuum spectral slope. We assume a linear relation between β and the luminosity (Bouwens et al. 2012; Tacchella, Trenti & Carollo 2013):

$$\langle\beta\rangle = \frac{{\rm d}\beta}{{\rm d}M_{\rm UV}}\left(M_{\rm UV,AB} + 19.5\right) + \beta_{M_{\rm UV}}, \quad (5)$$

We assume the same $\langle\beta\rangle$ as Arnouts et al. (2005), Oesch et al. (2010), Smit et al. (2012), Tacchella et al. (2013), Katsianis et al. (2017a), and Katsianis et al. (2017b).[7] Then, following Hao et al. (2011) we assume

$$\rm L_{UV-uncor} = L_{UV_{corr}} e^{-\tau_{UV}}, \quad (6)$$

where $\tau_{\rm UV}$ is the effective optical depth ($\tau_{\rm UV} = \rm A_{1600}/1.086$). We convert the dust-corrected UV luminosities into SFRs following Kennicutt & Evans (2012):

$$\rm Log_{10}(SFR) = Log_{10}(L_{UV_{corr}}) - 43.35. \quad (7)$$

We label the above as $\rm SFR_{UV\,+\,IRX-\beta}$.

All the above methods have been commonly used in the literature to derive SFRs but have different limitations. UV provides a direct measure of SFR, but could underestimate the total SFR due to dust

[4] $\rm Log_{10}(SFR_{TIR}) = Log_{10}(L_{TIR}) - 43.41$ $\rm Log_{10}(SFR_{FUV}) = Log_{10}(L_{FUV}) - 43.35$.

[5] The coefficients of the $L_{\rm TIR} = aL_{24\,\mu m} + bL_{70\,\mu m} + cL_{160\,\mu m}$ relation were derived from a singular value decomposition solution to an overdetermined set of linear equations. The equation matches the model bolometric infrared luminosities, for all model SED shapes, from 1 to 4 per cent at $z = 0$–4.

[6] The dust templates of Dale et al. (2014) are based on the same sample of nearby star-forming galaxies originally presented in Dale & Helou (2002).

[7] $\beta = -0.11(M_{\rm UV,\,AB} + 19.5) - 2.00$ at $z \simeq 4.0$ $\beta = -0.13(M_{\rm UV,\,AB} + 19.5) - 1.70$ at $z \simeq 2.0$ $\beta = -0.13(M_{\rm UV,\,AB} + 19.5) - 1.55$ at $z \simeq 1.0$

Table 1. The methodologies used to infer SFRs and stellar masses in the compilation of observations and EAGLE + SKIRT data used in this work. Stellar masses are typically inferred by the SED fitting technique, which employs various assumptions. In this work, we employ the Bruzual & Charlot (2003) models and assume an exponentially declining SFH [SFR = exp(-t/tau)] (Fumagalli et al. 2016; Abdurro'uf 2018), the Chabrier IMF (Chabrier 2003) with cut-offs at 0.1 and 100 $M_{\odot}$, the Calzetti et al. (2000) dust attenuation law (Cullen et al. 2018; McLure et al. 2018b), and a metallicity of 0.2 $Z_{\odot}$ (Chan et al. 2016; McLure et al. 2018a). These choices are typical among the observational studies used in this work. When necessary we convert the IMFs of the observed relations from Salpeter (1955) IMF to Chabrier (2003) IMF by decreasing the observed stellar masses by 0.21 dex (Davé 2008; Santini et al. 2012; Madau & Dickinson 2014; Katsianis et al. 2016) while SFR conversion laws are re-calibrated to Kennicutt & Evans (2012).

Authors/parent sample selection main-sequence selection	SFR	$M_{\star}$
	Observations	
Santini et al. (2009)/Optical–2σ Bruzual & Charlot (2003) models,	2700 Å + $IR_{24\,\mu m}$, Dale & Helou (2002) Salpeter (1955) IMF, exponentially declining SFHs	SED, Bruzual & Charlot (2003) Dust extinction, Calzetti et al. (2000), 1 $Z_{\odot}$
Kajisawa et al. (2010)/*K* band–$M_{\star}$ Bruzual & Charlot (2003)	2800 Å + SED dust Correction Salpeter (1955) IMF, exponentially declining SFHs	SED, GALAXEV (Bruzual & Charlot 2003) Dust extinction (Calzetti et al. 2000), 0.02–1 $Z_{\odot}$
Bauer et al. (2011)/*H* band–$M_{\star}$ Bruzual & Charlot (2003)	2800 Å + SED Calzetti et al. (2000) Salpeter (1955) IMF, exponentially declining SFHs	SED, HYPERZ Bolzonella et al. (2010) Dust extinction (Calzetti et al. 2000), 0.0001–0.05 $Z_{\odot}$
Heinis et al. (2014)/*i* band–UV Bruzual & Charlot (2003)	1600 Å + 250, 350, 500 μm, Dale & Helou (2002) Chabrier (2003) IMF, exponentially declining SFHs	SED, CIGALE Dust extinction, (Meurer et al. 1999)
Steinhardt et al. (2014)/UV–$M_{\star}$ Bruzual & Charlot (2003)	FIR, Casey (2012) Chabrier (2003) IMF, exponentially declining SFHs	SED, LePHARE (Arnouts & Ilbert 2011) Dust extinction (Calzetti et al. 2000), 0.5 $Z_{\odot}$
Whitaker et al. (2014)/IR–UVJ Bruzual & Charlot (2003)	2800 Å + $IR_{24\,\mu m}$,Wuyts et al. (2008) Chabrier (2003) IMF, rising + declining exponantially SFHs	SED, FAST Dust extinction, (Charlot & Fall 2000), 1 $Z_{\odot}$
Salmon et al. (2015)/photometric–$M_{\star}$ Bruzual & Charlot (2011),	Bayesian SED fitting Salpeter (1955) IMF, constant SFHs	Bayesian SED fitting Dust extinction (Charlot & Fall 2000), 0.2 $Z_{\odot}$
Tomczak et al. (2016)/*K* band–*UVJ* Bruzual & Charlot (2003)	2800 Å + $IR_{0.3-8\,\mu m}$, Wuyts et al. (2008) Chabrier (2003) IMF, exponentially declining SFHs	SED, FAST Dust extinction (Calzetti et al. 2000), 1 $Z_{\odot}$
Santini et al. (2017) *H* band–2σ Bruzual & Charlot (2003)	1600 Å + IRX–β, Meurer et al. (1999) Salpeter (1955) IMF, rising + declining delayed SFHs	SED, N/A Dust extinction (Calzetti et al. 2000), 0.02 $Z_{\odot}$
Pearson et al. (2018) *K* band–Gaussian Bruzual & Charlot (2003)	SED, CIGALE Chabrier (2003) IMF, exponantially delayed declining SFHs	SED, CIGALE Dust extinction (Charlot & Fall 2000), 0.02 $Z_{\odot}$
	EAGLE + SKIRT	
Fig. 2	SED, FAST	SED, FAST
Left-hand panels of Fig. 3	1600 Å + $IR_{24\,\mu m}$, Wuyts et al. (2008)	SED, FAST
Middle panels of Fig. 3	1600 Å + 24, 70, 160 μm, Dale & Helou (2002)	SED, FAST
Right-hand panels of Fig. 3	1600 Å + 250, 350, 500 μm, Dale et al. (2014)	SED, FAST
Fig. 4	1600 Å + IRX–β,Meurer et al. (1999)	SED, FAST
Figs 2, 3, and 4 (the dotted line)	SFR_{Int}	$M_{\star,\,Int}$

attenuation effects (Dunlop et al. 2017). IR wavelengths (especially mid-IR and far-IR) are used to determine the TIR luminosity, which is used to trace star formation. A major drawback of IR studies is that they usually do not have sufficient wavelength coverage especially at FIR wavelengths (Lee et al. 2013; Pearson et al. 2018). In order to overcome this limitation to determine the TIR luminosities, other authors have relied on extrapolations from the available wavebands (e.g. *Spitzer* 24 μm; Wuyts et al. 2008). However, the 24 μm band, mid-IR, and far-IR lumininosities can be compromised by AGN (Brand et al. 2006; Ichikawa et al. 2012; Roebuck et al. 2016; Brown et al. 2019). Even studies that have access to a range of IR wavelengths still have to rely on SED libraries (Dale & Helou 2002), which have been constructed from galaxies at low redshifts. These templates/models may not be representative for high-redshift objects. One other disadvantage of using TIR as a SFR tracer is that other sources can contribute to the heating of dust in galaxies and this contribution can be falsely interpreted as star formation. In particular, old stellar populations can significantly contribute to dust heating, complicating the relation between SFR and TIR emission (Bendo et al. 2010; Boquien et al. 2011; Bendo, Galliano & Madden 2012; Viaene et al. 2017; Nersesian et al. 2019). Due to the above limitations in the infrared other studies use SED fitting to bands beyond IR including UV wavelengths (Hunt et al. 2019; Leja et al. 2019). However, Santini et al. (2017) suggested that this method suffers from parameter degeneracies, which are serious for the SFR determination, and instead used dust-corrected UV luminosities in their analysis.

4 EAGLE + SKIRT VERSUS OBSERVATIONS

For the EAGLE + SKIRT galaxies in this work, we investigate all the above methods. The compilation of observations and different techninques used in this work is described in Table 1, while the results are summarized in Figs 2, 3, and 4, where we provide the number density plots of the inferred SFR–M⋆ plane and a comparison with observations (the density of points increases from white to dark blue). We note that the observations present at each panel alongside with the simulated results are derived following similar methods and wavelengths (Table 1). However, sample selection effects or unique assumptions for the SED modelling can be different from study to study and exploring these variations is beyond the scope of our current work.

(i) The black solid lines in the panels in Fig. 2 represent the median $\mathrm{SFR_{SED-FAST}}$-$\mathrm{M_{\star,\,SED-FAST}}$ relation at $z \simeq 4$ (top), $z \simeq 2$ (middle), and $z \simeq 1$ (bottom). The derived relation (the solid black line) has an offset in SFR at a given $\mathrm{M_\star}$ with respect the intrinsic relation (the dotted black line) at all redshifts considered (Fig. 2 and Table 2, offset $_{z\simeq4} \sim -0.2$ to -0.5 dex, offset $_{z\simeq2} \simeq -0.15$ to 0, and offset $_{z\simeq1} \simeq 0.2$ to 0.5 dex) and appears to be flatter at $z \simeq 4$ but steeper at $z \simeq 1$ than the intrinsic slope. In Appendix A, we demonstrate that the above is the result of underpredicted SFRs at $z \sim 4$ and underpredicted stellar masses and overpredicted SFRs at $z = 1$. The green squares represent the observations of Kajisawa et al. (2010), Bauer et al. (2011), and Salmon et al. (2015), while the dashed green lines describe the results of Pearson et al. (2018). Kajisawa et al. (2010) determined the SFRs of GOODS-North galaxies using dust corrections inferred from SED fitting to the *UBV*$_{iz}$*JHK*, 3.6, 4.5, and 5.8 μm bands alongside with 2800 Å luminosities and the Kennicutt (1998) relation. Bauer et al. (2011) derived the SFRs of the GOODS–NICMOS galaxies using their UV luminosities and dust corrections inferred from SED fitting (Calzetti et al. 2000; Bruzual & Charlot 2003). Salmon et al. (2015) retrieved SFRs from the CANDELS and *Spitzer* Extended Deep Survey. The authors used a Bayesian SED fitting procedure taking advantage of mock catalogues and synthetic photometry from semi-analytic models. Pearson et al. (2018) obtained the SFRs and stellar masses of the COSMOS galaxies using the CIGALE SED fitting code and assumed delayed exponentially declining SFHs, the Bruzual & Charlot (2003) stellar population synthesis model and the Charlot & Fall (2000) dust attenuation. The above authors used SED fitting methods to derive properties of galaxies and despite small differences in their assumptions (for more details present see Table 1) produce similar results. The observational SFR–$\mathrm{M_\star}$ and the EAGLE + SKIRT $\mathrm{SFR_{SED-FAST}}$-$\mathrm{M_{\star,\,SED-FAST}}$ are in good agreement at $z \simeq$ 1–2 but not at redshift $z \simeq 4$ where the $\mathrm{SFR_{SED-FAST}}$-$\mathrm{M_{\star,\,SED-FAST}}$ relation implies lower values of SFR at fixed stellar mass than observed by $\simeq$0.2 to 0.5 dex. Nevertheless, we see already that the assumed methodology to obtain intrinsic properties can have a considerable effect to the derived SFR–$\mathrm{M_\star}$ relation.

(ii) The solid black lines in the left-hand panels of Fig. 3 represent the $\mathrm{SFR_{24\,\mu m-Wuyts\,et\,al.\,2008}}$–$\mathrm{M_{\star,\,SED-FAST}}$ relation at $z \simeq$ 4 (top), $z \simeq 2$ (middle), and $z \simeq 1$ (bottom). The inferred relation (the solid black line) is offset to higher SFRs than the intrinsic relation (the dotted black line) at all redshifts considered (Fig. 3 and Table 2, offset $_{z\simeq4} \simeq$ 0.30–0.44 dex, offset$_{z\simeq2} \simeq 0.3$, and offset $_{z\simeq1} \simeq 0.25$ dex). In Appendix A, we demonstrate that this is the result of underpredicted stellar masses and overpredicted SFRs. The orange squares in the right-hand panels of Fig. 3 represent the results of Whitaker et al. (2014) who adopted a luminosity-independent conversion from the observed $\mathrm{IR_{24\,\mu m}}$ flux density to

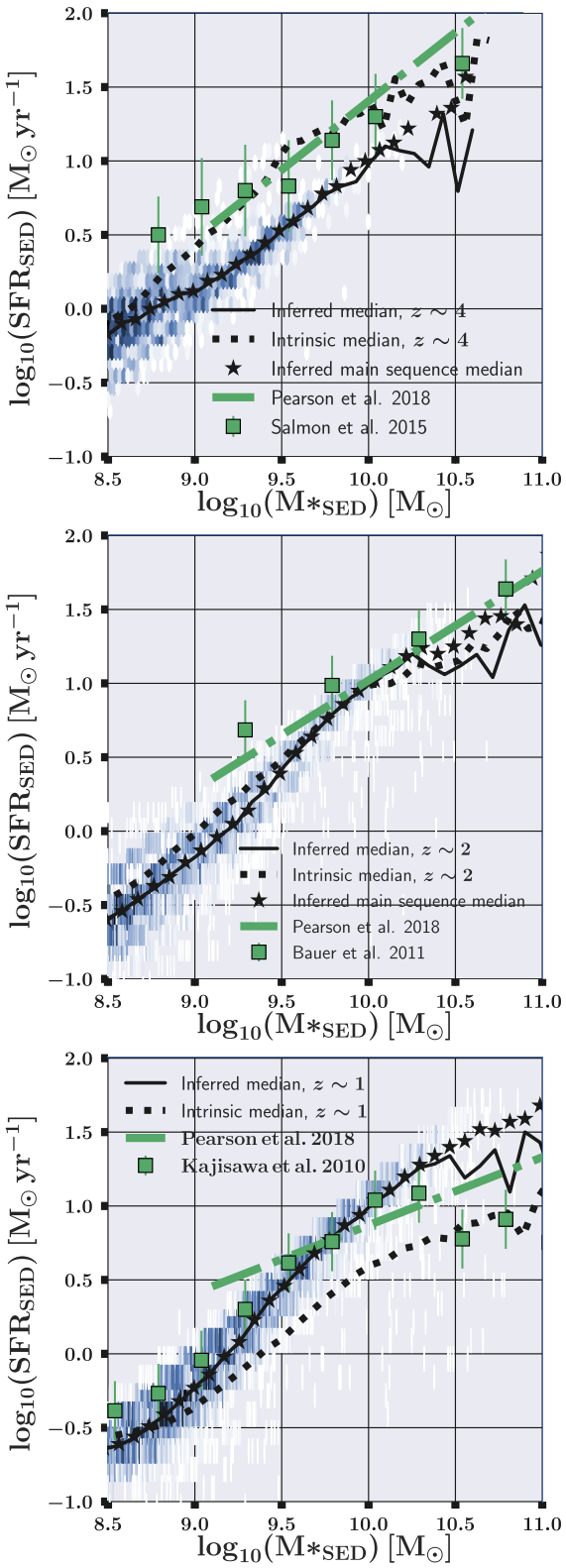

Figure 2. The black solid curves show the median SFR−$\mathrm{M_\star}$ relation using SED fitting (Kriek et al. 2009) to infer SFRs and stellar masses. The dotted line represents the intrinsic relation for the same galaxies ($\mathrm{SFR_{Intr}}$−$\mathrm{M_{\star,\,Intr}}$). The black stars represent the inferred main-sequence relation defined by the exclusion of passive objects with sSFR $< 10^{-9.1}$ at $z \sim 4$, sSFR $< 10^{-9.6}$ at $z \sim 2$, and sSFR $< 10^{-10.1}$ at $z \sim 1$.

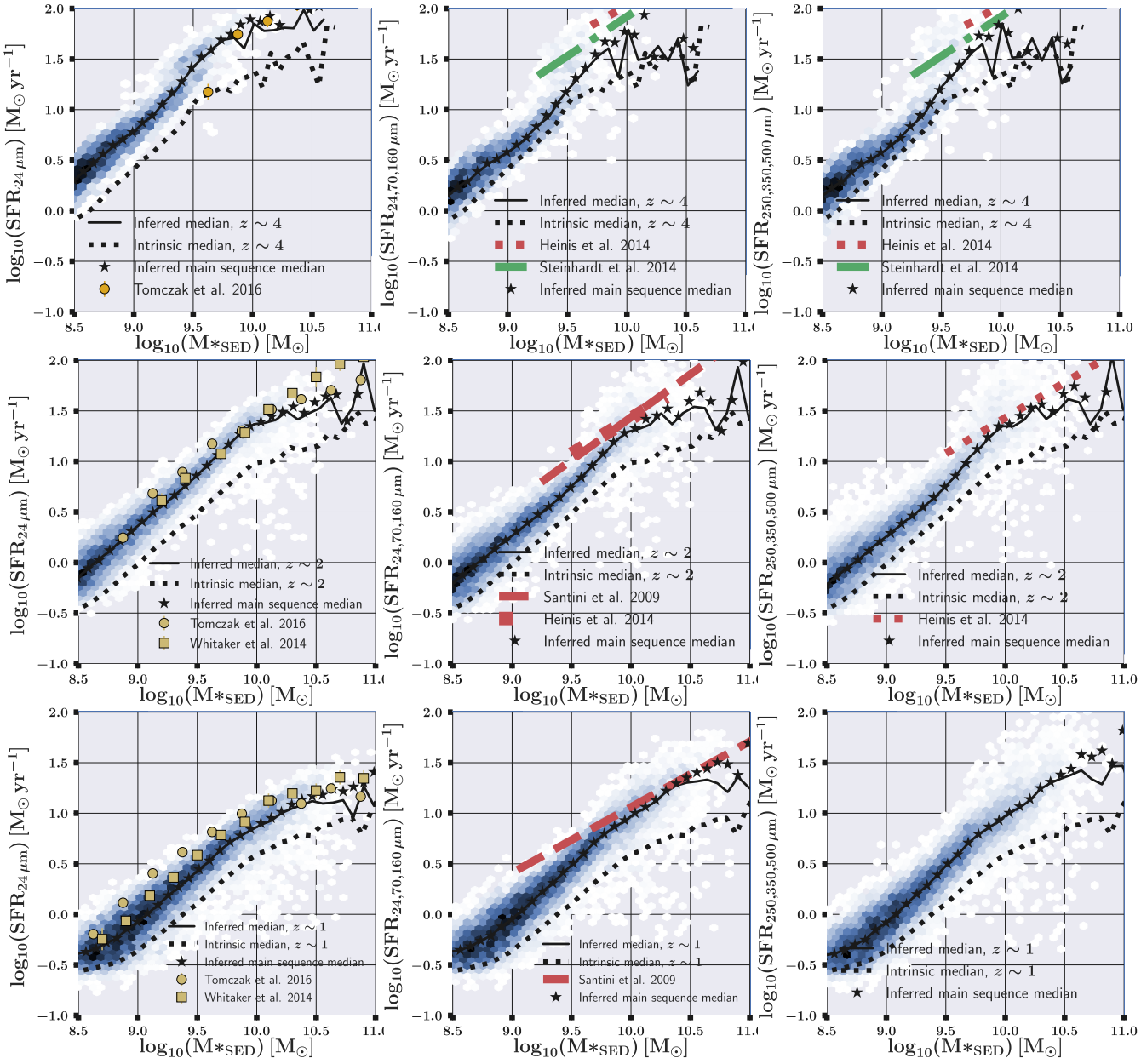

Figure 3. The evolution of the SFR−M$_\star$ relation using the EAGLE + SKIRT data using IR wavelengths. The black solid and dotted curves show the median relation inferred from the mock EAGLE + SKIRT observations, while the black dotted line represents the intrinsic relation (SFR$_{\rm Intr}$−M$_{\star,\,\rm Intr}$) for the same galaxies. The colour scale indicates the number density of the EAGLE + SKIRT galaxies in the SFR−M$_\star$ plane. Different rows show different redshifts. Left-hand panels: SFRs are calculated adopting the luminosity-independent conversion from the observed *Spitzer*/MIPS 24 μm flux density to the total IR luminosity following (Wuyts et al. 2008). Stellar masses are calculated using the Fitting and Assessment of Synthetic Templates (FAST) code (Kriek et al. 2009). Middle panels: Star formation rates are calculated using the 24, 70, and 160 μm luminosities and their relation with the total IR luminosity given by the Dale & Helou (2002) templates and the TIR–SFR conversion given by Kennicutt & Evans (2012). Right-hand panels: Star formation rates are calculated using the 250, 350, and 500 μm luminosities, the Dale et al. (2014) templates and the conversion given by Kennicutt & Evans (2012). The tension between observed and simulated SFR−M$_\star$ relations is generally highly reduced if both SFR and stellar masses are retrieved using similar methods in observations and simulations. In Table 2, we summarize the offset between the intrinsic and inferred relations at different mass bins. The black stars represent the inferred main-sequence relation defined by the exclusion of passive objects with $sSFR < 10^{-9.1}$ at $z \sim 4$, $sSFR < 10^{-9.6}$ at $z \sim 2$, and $sSFR < 10^{-10.1}$ at $z \sim 1$.

the TIR luminosity following Wuyts et al. (2008) and the 2800 Å emission of 39 106 star-forming galaxies selected from the 3D-HST photometric catalogues. The orange circles show the results of Tomczak et al. (2016) who used data from the ZFOURGE survey combined with IR imaging from the *Spitzer* and *Herschel* observatories. The authors inferred stellar masses by fitting stellar population synthesis templates (Bruzual & Charlot 2003) to the 0.3–8 μm photometry using the SED-fitting code FAST (Kriek et al. 2009) assuming a Chabrier (2003) IMF, solar metallicity, and exponentially declining SFHs alongside with a Calzetti et al. (2000) extinction law. SFRs were derived by combining UV and TIR luminosities, where TIR were inferred using the Wuyts et al.

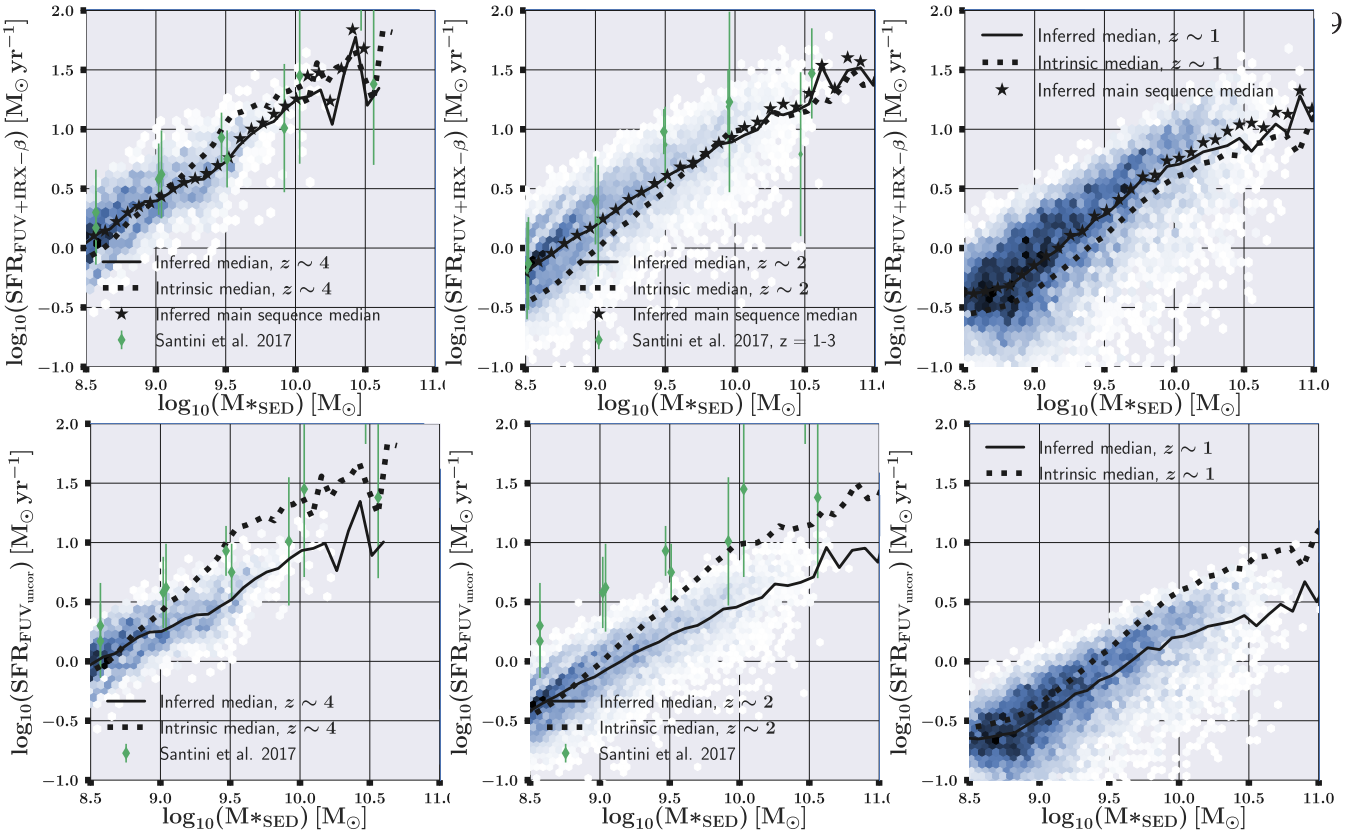

Figure 4. Top panels: Same as Fig. 3, but for SFRs derived from the FUV luminosity (Kennicutt & Evans 2012) and the IRX–β relation (Meurer et al. 1999; Bouwens et al. 2012; Katsianis et al. 2017a), while the stellar masses are calculated through the SED fitting technique (the black solid line). When applied to the EAGLE + SKIRT data, this method yields a relation that is slightly flatter than the intrinsic (the black dotted line). Bottom panels: Same as top but instead dust corrections are not applied.

Table 2. The offset in dex between the derived and intrinsic SFR–$M_\star$ relations at different masses. To infer the intrinsic relation a decrement equal to the offset we report is required.

Methodology	$10^{8.5}$	$10^{9.0}$	$10^{9.5}$ Offset	10^{10} (dex)	$10^{10.5}$	$10^{11.0}$
$SFR_{SED-FAST}$ - $M_{\star,\,SED-FAST}$, $z = 4$	−0.10	−0.30	−0.58	−0.38	−0.35	–
$SFR_{SED-FAST}$ - $M_{\star,\,SED-FAST}$, $z = 2$	−0.10	−0.12	−0.06	−0.01	−0.01	−0.04
$SFR_{SED-FAST}$ - $M_{\star,\,SED-FAST}$, $z = 1$	−0.01	0.16	0.26	0.43	0.56	0.07
$SFR_{24\,\mu m-Wuyts\,et\,al.\,2008}$ - $M_{\star,\,SED-FAST}$, $z = 4$	0.46	0.37	0.31	0.46	0.54	–
$SFR_{24\,\mu m-Wuyts\,et\,al.\,2008}$ - $M_{\star,\,SED-FAST}$, $z = 2$	0.38	0.32	0.32	0.39	0.37	0.04
$SFR_{24\,\mu m-Wuyts\,et\,al.\,2008}$ - $M_{\star,\,SED-FAST}$, $z = 1$	0.18	0.31	0.34	0.28	0.22	−0.02
$SFR_{24,70,160\,\mu m-r\,Dale\&Helou\,2002}$ - $M_{\star,\,SED-FAST}$, $z = 4$	0.31	0.09	0.10	0.49	−0.01	–
$SFR_{24,70,160\,\mu m-r\,Dale\&Helou\,2002}$ - $M_{\star,\,SED-FAST}$, $z = 2$	0.32	0.32	0.20	0.33	0.38	−0.01
$SFR_{24,70,160\,\mu m-r\,Dale\&Helou\,2002}$ - $M_{\star,\,SED-FAST}$, $z = 1$	0.19	0.34	0.30	0.40	0.43	−0.02
$SFR_{250,350,500\,\mu m-c\,Dale\&Helou\,2014}$ - $M_{\star,\,SED-FAST}$, $z = 4$	0.22	0.16	0.11	0.47	0.06	–
$SFR_{250,350,500\,\mu m-c\,Dale\&Helou\,2014}$ - $M_{\star,\,SED-FAST}$, $z = 2$	0.22	0.31	0.20	0.35	0.46	−0.07
$SFR_{250,350,500\,\mu m-c\,Dale\&Helou\,2014}$ - $M_{\star,\,SED-FAST}$, $z = 1$	0.16	0.31	0.40	0.40	0.56	−0.01
$SFR_{UV+IRX-\beta}$ - $M_{\star,\,SED-FAST}$, $z = 4$	0.11	−0.02	−0.13	−0.04	−0.02	–
$SFR_{UV+IRX-\beta}$ - $M_{\star,\,SED-FAST}$, $z = 2$	0.23	0.16	0.04	−0.02	−0.01	−0.02
$SFR_{UV+IRX-\beta}$ - $M_{\star,\,SED-FAST}$, $z = 1$	0.17	0.22	0.19	0.10	−0.02	−0.08

(2008) templates. The observational SFR–$M_\star$ relations are in good agreement with the predicted $SFR_{24\,\mu m-Wuyts\,et\,al.\,2008}$–$M_{\star,\,SED-FAST}$ from the EAGLE + SKIRT data. The agreement improves further if an MS is specified (the black stars) defined by excluding passive objects imposing a redshift specific SFR cut (Furlong et al. 2015; Schaye et al. 2015; Katsianis et al. 2019; Matthee & Schaye 2019): $sSFR < 10^{-9.1}$ at $z \sim 4$, $sSFR < 10^{-9.6}$ at $z \sim 2$, and $sSFR < 10^{-10.1}$ at $z \sim 1$.

(iii) The black solid lines in the middle panels of Fig. 3 represent the $SFR_{24,70,160\,\mu m-r\,Dale\&Helou\,2002}$–$M_{\star,\,SED-FAST}$ relation at $z \simeq 4$ (top), $z \simeq 2$ (middle), and $z \simeq 1$ (bottom) retrieved from the EAGLE + SKIRT data. The dotted black line represents the

intrinsic/true relation from the same sample. The inferred relation (the solid black line), implies larger SFRs at fixed stellar mass than the intrinsic relation (the dotted black line) at all redshifts considered, for masses in the $\log_{10}(M_\star/\mathrm{M}_\odot) \simeq 8.5-10.0$ range (Fig. 3 and Table 2, offset $_{z\simeq4} \simeq 0.1$–0.5 dex, offset $_{z\simeq2} \simeq 0.2-0.4$ and offset $_{z\simeq1} \simeq 0.2-0.4$ dex). In the Appendix A, we demonstrate that this is the result of overpredicted SFRs (by up to 0.3 dex at $z \simeq 2$) and underpredicted stellar masses (by up to -0.20 dex at $z \simeq 2$).[8] We also plot the observations of Santini et al. (2009; the red-dashed lines), Heinis et al. (2014; the red-dotted lines), and Steinhardt et al. (2014; the green-dashed line). Santini et al. (2009) inferred the TIR of the GOODS-MUSIC galaxies using their 24 μm luminosities and the Dale & Helou (2002) templates and combined the above TIR luminosities with UV emission (2700 Å) in order to derive the galaxy SFRs. Steinhardt et al. (2014) used the far-IR *Herschel* wavelengths and employed the Casey (2012) models, which are very similar to the Dale & Helou (2002) templates. The SFR $_{24,70,160\,\mu\mathrm{m}-\mathrm{r\,Dale\&Helou\,2002}}$–$\mathrm{M}_{\star,\,\mathrm{SED-FAST}}$ relation derived from EAGLE + SKIRT simulations is in agreement with observations.

(iv) The black solid lines in the right-hand panels of Fig. 3 represent the SFR $_{250,350,500\,\mu\mathrm{m}-\mathrm{c\,Dale\&Helou\,2014}}$–$\mathrm{M}_{\star,\,\mathrm{SED-FAST}}$ relation at $z \simeq 4$ (top), $z \simeq 2$ (middle), and $z \simeq 1$ (bottom) retrieved from the EAGLE + SKIRT data. Similarly with the middle panel, in which the SFR $_{24,70,160\,\mu\mathrm{m}-\mathrm{r\,Dale\&Helou\,2002}}$–$\mathrm{M}_{\star,\,\mathrm{SED-FAST}}$ is described, the inferred relation (the solid black line) implies larger SFRs at fixed stellar mass than the intrinsic relation (the otted black line) at all redshifts considered, for masses in the $\log_{10}(M_\star/\mathrm{M}_\odot) \simeq 8.5-10.5$ range (Fig. 3 and Table 2).

(v) The top black solid lines in Fig. 4 represent the $\mathrm{SFR}_{\mathrm{UV+IRX}-\beta}$-$\mathrm{M}_{\star,\,\mathrm{SED-FAST}}$ relation at $z \simeq 4$ (left), $z \simeq 2$ (middle), and $z \simeq 1$ (right).[9] The derived relation (the black solid line) has an offset with respect to the intrinsic relation (the black-dotted line) of offset $_{z\simeq4} \simeq 0.11$ to -0.13 dex, offset $_{z\simeq2} \simeq 0.23$ to -0.02, and offset $_{z\simeq1} \simeq 0.22$ to -0.08 dex (Fig. 4 and Table 2). At $z \sim 4$ for masses in the $\log_{10}(M_\star/\mathrm{M}_\odot) \simeq 8.5-9$ range, the SFRs are typically overestimated. However, the SFRs are underestimated for $\log_{10}(M_\star/\mathrm{M}_\odot) > 9.5$. This makes the inferred $\mathrm{SFR}_{\mathrm{UV+IRX}-\beta}$–$\mathrm{M}_{\star,\,\mathrm{SED-FAST}}$ relation flatter. Santini et al. (2017) inferred the SFR–$\mathrm{M}_\star$ relation for the *Hubble Space Telescope* Frontier fields galaxies, based on rest-frame UV observations, the Kennicutt & Evans (2012) relation and the Meurer et al. (1999) dust correction law. We see that both the derived $\mathrm{SFR}_{\mathrm{UV+IRX}-\beta}$–$\mathrm{M}_{\star,\,\mathrm{SED-FAST}}$ (the black solid line) and $\mathrm{SFR}_{\mathrm{Intr}}$–$\mathrm{M}_{\star,\,\mathrm{Intr}}$ (the black dotted line) relations are consistent with the observations. A common finding for all redhifts of interest is that the derived relation is flatter than the intrinsic.

In Fig. 5, we present the offset in dex with respect the intrinsic/true EAGLE + SKIRT relation for all methodologies used to derive the SFR−$\mathrm{M}_\star$ relation from the EAGLE + SKIRT data at $z \simeq 4$ (top), $z \simeq 2$ (middle), and $z \simeq 1$ (bottom). The dark green dot–dashed line represents the offset of the SFR−$\mathrm{M}_\star$ calculated using the FAST SED fitting code. The orange dash–dotted line represents the SFRs that are inferred from FUV and $\mathrm{IR}_{24\,\mu\mathrm{m}}$ luminosities (Wuyts et al. 2008). The magenta solid line

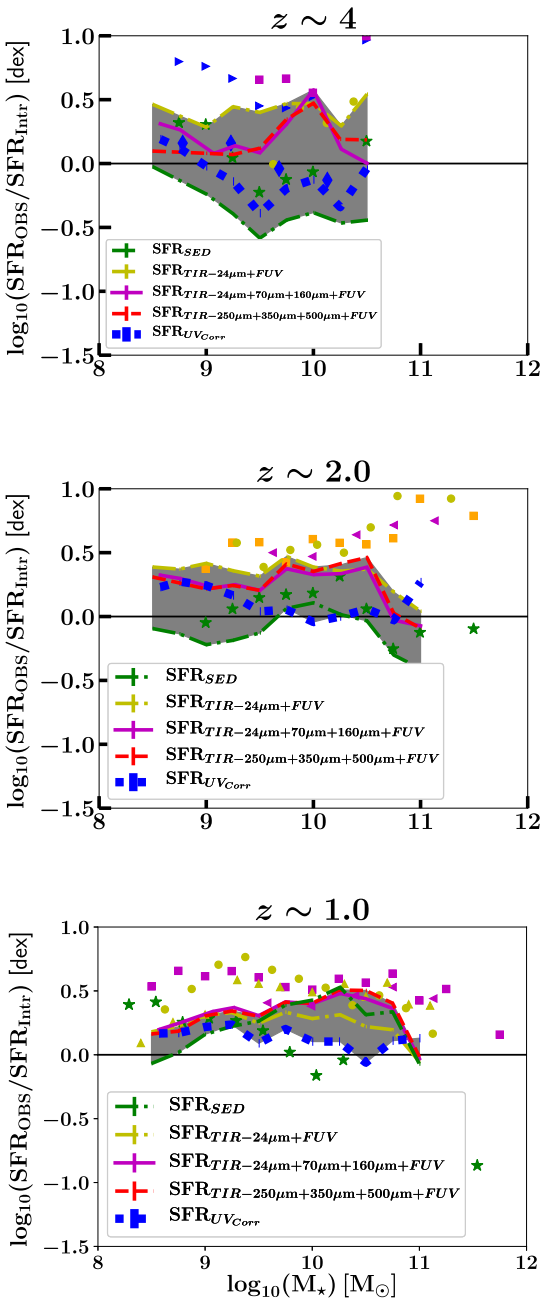

Figure 5. The offset in dex between the various methods used to derive the SFR−$\mathrm{M}_\star$ relation from the mock EAGLE + SKIRT data with respect the intrinsic EAGLE relation (the solid 0 dex line) at $z \simeq 4$ (top), $z \simeq 2$ (medium), and $z \simeq 1$ (bottom). The dark-green-dashed line represents the offset of the SFR−M⋆ calculated using the FAST SED fitting code. The orange dash–dotted line represents the SFRs that are inferred from FUV and $\mathrm{IR}_{24\,\mu\mathrm{m}}$ luminosities (Wuyts et al. 2008). The magenta solid line represents the results when SFRs are calculated using the 24, 70, and 160 μm luminosities and the relation given by the Dale & Helou (2002) templates. The red-dashed line represents the results when SFRs are calculated using the 250, 350, and 500 μm luminosities and the Dale et al. (2014) templates. The blue-dotted line describes the SFRs derived from UV luminosities dust-corrected using the IRX–β relation (Meurer et al. 1999). The grey area describes the offset in dex between the range of methodologies used in this work that spans areas of ~ 0.5–1 dex at $z = 4$, ~ 0.5 dex at $z = 2$, and ~ 0.1–0.5 dex at $z = 1$. We see that the level of discrepancy between different methodologies produced by the EAGLE + SKIRT data resembles that of those observed relations reported in the literature.

[8] We note that an overprediction/underprediction of the retrieved SFRs shifts the relation to higher/lower normalizations, while an overprediction/underpredction of stellar masses shifts the SFR–$\mathrm{M}_\star$ relation to lower/higher SFRs at a fixed stellar mass.

[9] In order to demonstrate the effect of dust corrections, we present the relation if UV light is dust uncorrected at the bottom panel.

represents the SFR $_{24,70,160\,\mu m-r\,Dale\&Helou\,2002}$–$M_{\star,\,SED-FAST}$ versus SFR_{Intr}–M_{Intr} relation. The red-dashed line represents the SFR $_{250,350,500\,\mu m-c\,Dale\&Helou\,2014}$–$M_{\star,\,SED-FAST}$ versus SFR_{Intr}–M_{Intr} relation. The blue-dotted line represents the $SFR_{UV+IRX-\beta}$–$M_{\star,\,SED-FAST}$ relation. The grey area encompasses the offset between the range of different methodologies used in this work. The results span areas of ~ 0.5 to 1.0 dex at $z \sim 4$, 0.5 dex at $z \sim 2$ and 0.1 to 0.5 dex at $z \sim 1$. Alongside, we present the observed relations shown in Fig. 1 in order to demonstrate that a similar level of tension exists between them. Thus, considering the comparisons present at Figs 2, 3, 4, and 5, we suggest that the discrepancies between observational studies have largely their roots in the diversity of methodologies used in the literature to derive SFRs (Katsianis et al. 2016). We note that the tension represented by the grey area reported above, reproduced by the EAGLE + SKIRT data, has its roots solely in differences in SFR determinations since stellar masses are in all cases computed with the same technique. A further future analysis that explores selection effects to the SFR−$M_\star$ relations employing mock observations can probably be used to supplementary address the tension between observations in the literature.

5 DISCUSSION AND CONCLUSIONS

Significant tension has been reported between observed high-redshift SFR–stellar mass ($M_\star$) relations reported by different authors in terms of normalization, shape, and slope (Section 2). We examined the SFR–$M_\star$ relation of $z \simeq 1$–4 galaxies using the SKIRT simulated SEDs (Camps et al. 2018) from the EAGLE hydrodynamic simulations. We derived SFRs and stellar masses using different observational techniques (e.g. SED fitting, UV + TIR luminosities, IR_{24} data, and UV + IRX–β relation). We compared our results from the simulated data with a range of observed relations and revisited the inconsistency reported between observed and simulated SFR–M∗ relations in the literature (e.g. Sparre et al. 2015; Katsianis et al. 2016). Our main findings are

(i) the tension between the observed and simulated SFR–$M_\star$ relations at $z \simeq 1$–4 can be largely alleviated. The discrepancy is decreased considerably when methodological biases, associated with estimating SFR and $M_\star$ from observations, are taken into account (Section 4, Figs 2, 3, and 4).

(ii) SFRs derived from combinations of Infrared wavelengths (e.g. 24, 24, 70, and 160 μm or 250, 350, and 500 μm) with UV luminosities are significantly overestimated with respect to the intrinsic values by 0.2–0.5 dex (at $z \simeq 1$–4) for the $\log_{10}(M_\star/M_\odot) \simeq 8.5-10.5$ range. The above results in significantly high normalizations for the $SFR_{24\,\mu m-Wuyts\,et\,al.\,2008}$–$M_{\star,\,SED-FAST}$, $SFR_{24,70,160\,\mu m-r\,Dale\&Helou\,2002}$–$M_{\star,\,SED-FAST}$ and $SFR_{250,350,500\,\mu m-c\,Dale\&Helou\,2014}$–$M_{\star,\,SED-FAST}$. On the other hand, $SFR_{UV+IRX-\beta}$–$M_{\star,\,SED-FAST}$ relations that rely on SFRs inferred solely from dust-corrected UV luminosities are flatter with deviations from the intrinsic values of up to −0.13 dex at $z \simeq 4$. We find that the normalization of $SFR_{SED-FAST}$–$M_{\star,\,SED-FAST}$ is significantly underestimated by up to −0.58 dex at $z \simeq 4$ but overestimated by up to 0.3 dex at $z \sim 1$ (Section 4, Figs 2, 3, and 4).

(iii) The tension between different observational studies (up to 0.8 dex at $z \simeq 4$ and up to 0.5 dex at $z \simeq 1$, Section 2.1) is at a great extent driven by the different techniques used by different groups to derive observational SFRs (Section 4, Fig. 5) with significant redshift dependence on the level of misestimation.

ACKNOWLEDGEMENTS

This work used the DiRAC Data Centric system at Durham University, operated by the Institute for Computational Cosmology on behalf of the STFC DiRAC HPC Facility (www.dirac.ac.uk). AK has been supported by the *Tsung-Dao Lee Institute Fellowship, Shanghai Jiao Tong University,* and *CONICYT/FONDECYT fellowship, project number: 3160049*. XY is supported by the national science foundation of China (grant nos. 11833005, 11890692, and 11621303) and Shanghai Natural Science Foundation, grant no. 15ZR1446700. We also thank the support of the Key Laboratory for Particle Physics, Astrophysics and Cosmology, and Ministry of Education. CL has received funding from the ARC Centre of Excellence for All Sky Astrophysics in 3 Dimensions (ASTRO 3D), through project number CE170100013. Cosmic Dawn Centre is funded by the Danish National Research Foundation. MS acknowledges support by the Ministry of Education, Science and Technological Development of the Republic of Serbia through the projects Astrophysical Spectroscopy of Extragalactic Objects (176001) and Gravitation and the Large-Scale Structure of the Universe (176003). We would like to thank the anonymous referee for the suggestions and comments that significantly improved our work.

REFERENCES

Abdurro'uf M. A., 2018, MNRAS, 479, 5083
Adachi M., Kasai M., 2012, Prog. Theor. Phys., 127, 145
Aird J., Coil A. L., Georgakakis A., 2018, MNRAS, 474, 1225
Arnouts S., Ilbert O., 2011, Astrophysics Source Code Library, record ascl:1108.009
Arnouts S. et al., 2005, ApJ, 619, L43
Artale M. C., Mapelli M., Giacobbo N., Sabha N. B., Spera M., Santoliquido F., Bressan A., 2019, MNRAS, 487, 1675
Baes M. et al., 2003, MNRAS, 343, 1081
Baes M., Verstappen J., De Looze I., Fritz J., Saftly W., Vidal Pérez E., Stalevski M., Valcke S., 2011, ApJS, 196, 22
Baes M., Camps P., Van De Putte D., 2017, MNRAS, 468, 927
Baes M., Trčka A., Camps P., Nersesian A., Trayford J., Theuns T., Dobbels W., 2019, MNRAS, 484, 4069
Bauer A. E., Conselice C. J., Pérez-González P. G., Grützbauch R., Bluck A. F. L., Buitrago F., Mortlock A., 2011, MNRAS, 417, 289
Bendo G. J. et al., 2010, A&A, 518, L65
Bendo G. J., Galliano F., Madden S. C., 2012, MNRAS, 423, 197
Bendo G. J. et al., 2015, MNRAS, 448, 135
Bisigello L., Caputi K. I., Grogin N., Koekemoer A., 2018, A&A, 609, A82
Blanc G. A., Lu Y., Benson A., Katsianis A., Barraza M., 2019, ApJ, 877, 6
Bolzonella M. et al., 2010, A&A, 524, A76
Boquien M. et al., 2011, AJ, 142, 111
Boquien M., Buat V., Perret V., 2014, A&A, 571, A72
Boquien M., Burgarella D., Roehlly Y., Buat V., Ciesla L., Corre D., Inoue A. K., Salas H., 2019, A&A, 622, A103
Boselli A. et al., 2010, PASP, 122, 261
Botticella M. T. et al., 2017, A&A, 598, A50
Bouwens R. J. et al., 2012, ApJ, 754, 83
Bouwens R. J. et al., 2015, ApJ, 803, 34
Brand K. et al., 2006, ApJ, 644, 143
Brinchmann J., Charlot S., White S. D. M., Tremonti C., Kauffmann G., Heckman T., Brinkmann J., 2004, MNRAS, 351, 1151
Brinchmann J., Charlot S., Kauffmann G., Heckman T., White S. D. M., Tremonti C., 2013, MNRAS, 432, 2112
Brown A., Nayyeri H., Cooray A., Ma J., Hickox R. C., Azadi M., 2019, ApJ, 871, 87
Brown T. M., Ferguson H. C., Smith E., Bowers C. W., Kimble R. A., Renzini A., Rich R. M., 2003, ApJ, 584, L69
Bruzual G., Charlot S., 2003, MNRAS, 344, 1000

Bruzual G., Charlot S., 2011, Astrophysics Source Code Library, record ascl:1104.005
Calzetti D., Armus L., Bohlin R. C., Kinney A. L., Koornneef J., Storchi-Bergmann T., 2000, ApJ, 533, 682
Camps P., Baes M., 2015, Astron. Comput., 9, 20
Camps P., Trayford J. W., Baes M., Theuns T., Schaller M., Schaye J., 2016, MNRAS, 462, 1057
Camps P. et al., 2018, ApJS, 234, 20
Cano-Díaz M., Ávila-Reese V., Sánchez S. F., Hernández-Toledo H. M., Rodríguez-Puebla A., Boquien M., Ibarra-Medel H., 2019, MNRAS, 1830
Casey C. M., 2012, MNRAS, 425, 3094
Chabrier G., 2003, PASP, 115, 763
Chan J. C. C. et al., 2016, MNRAS, 458, 3181
Charlot S., Fall S. M., 2000, ApJ, 539, 718
Cohen M., Wheaton W. A., Megeath S. T., 2003, AJ, 126, 1090
Conroy C., 2013, ARA&A, 51, 393
Cortese L. et al., 2012, A&A, 540, A52
Cowley W. I., Lacey C. G., Baugh C. M., Cole S., Frenk C. S., Lagos C. d. P., 2019, MNRAS, 487, 3082
Crain R. A. et al., 2015, MNRAS, 450, 1937
Cullen F. et al., 2018, MNRAS, 476, 3218
Daddi E. et al., 2007, ApJ, 670, 156
Daddi E. et al., 2009, ApJ, 694, 1517
Daddi E., Cimatti A., Renzini A., Fontana A., Mignoli M., Pozzetti L., Tozzi P., Zamorani G., 2004, ApJ, 617, 746
Dale D. A., Helou G., 2002, ApJ, 576, 159
Dale D. A., Helou G., Magdis G. E., Armus L., Díaz-Santos T., Shi Y., 2014, ApJ, 784, 83
Dalla Vecchia C., Schaye J., 2012, MNRAS, 426, 140
Davé R., 2008, MNRAS, 385, 147
Davies L. J. M. et al., 2016, MNRAS, 461, 458
Davies L. J. M. et al., 2017, MNRAS, 466, 2312
Davies L. J. M. et al., 2019, MNRAS, 483, 1881
de Barros S., Schaerer D., Stark D. P., 2014, A&A, 563, A81
De Looze I. et al., 2014, A&A, 568, A62
Doi M. et al., 2010, AJ, 139, 1628
Donnari M. et al., 2019, MNRAS, 485, 4817
Drory N., Alvarez M., 2008, ApJ, 680, 41
Dunlop J. S. et al., 2017, MNRAS, 466, 861
Dunne L. et al., 2009, MNRAS, 394, 3
Dutton A. A., van den Bosch F. C., Dekel A., 2010, MNRAS, 405, 1690
Elbaz D. et al., 2007, A&A, 468, 33
Elbaz D. et al., 2011, A&A, 533, A119
Espada D. et al., 2019, ApJ, 887, 88
Franx M., van Dokkum P. G., Förster Schreiber N. M., Wuyts S., Labbé I., Toft S., 2008, ApJ, 688, 770
Fumagalli M. et al., 2014, ApJ, 796, 35
Fumagalli M. et al., 2016, ApJ, 822, 1
Furlong M. et al., 2015, MNRAS, 450, 4486
González V., Bouwens R. J., Labbé I., Illingworth G., Oesch P., Franx M., Magee D., 2012, ApJ, 755, 148
Griffin M. J. et al., 2010, A&A, 518, L3
Groves B., Dopita M. A., Sutherland R. S., Kewley L. J., Fischera J., Leitherer C., Brandl B., van Breugel W., 2008, ApJS, 176, 438
Guo K., Zheng X. Z., Fu H., 2013, ApJ, 778, 23
Guo K., Zheng X. Z., Wang T., Fu H., 2015, ApJ, 808, L49
Hao C.-N., Kennicutt R. C., Johnson B. D., Calzetti D., Dale D. A., Moustakas J., 2011, ApJ, 741, 124
Hayward C. C., Smith D. J. B., 2015, MNRAS, 446, 1512
Hayward C. C. et al., 2014, MNRAS, 445, 1598
Heinis S. et al., 2014, MNRAS, 437, 1268
Helou G., Lu N. Y., Werner M. W., Malhotra S., Silbermann N., 2000, ApJ, 532, L21
Hunt L. K. et al., 2019, A&A, 621, A51
Ichikawa K., Ueda Y., Terashima Y., Oyabu S., Gandhi P., Matsuta K., Nakagawa T., 2012, ApJ, 754, 45
Jenkins A., 2010, MNRAS, 403, 1859
Kajisawa M., Ichikawa T., Yamada T., Uchimoto Y. K., Yoshikawa T., Akiyama M., Onodera M., 2010, ApJ, 723, 129
Karim A. et al., 2011, ApJ, 730, 61
Kashino D. et al., 2013, ApJ, 777, L8
Katsianis A., Tescari E., Wyithe J. S. B., 2015, MNRAS, 448, 3001
Katsianis A., Tescari E., Wyithe J. S. B., 2016, Publ. Astron. Soc. Aust., 33, e029
Katsianis A., Tescari E., Blanc G., Sargent M., 2017a, MNRAS, 464, 4977
Katsianis A. et al., 2017b, MNRAS, 472, 919
Katsianis A. et al., 2019, ApJ, 879, 11
Kennicutt R. C., Jr., 1998, ARA&A, 36, 189
Kennicutt R. C., Evans N. J., 2012, ARA&A, 50, 531
Kitzbichler M. G., White S. D. M., 2007, MNRAS, 376, 2
Kriek M., van Dokkum P. G., Labbé I., Franx M., Illingworth G. D., Marchesini D., Quadri R. F., 2009, ApJ, 700, 221
Kurczynski P. et al., 2016, ApJ, 820, L1
Lagos C. d. P. et al., 2015, MNRAS, 452, 3815
Lagos C. d. P., Theuns T., Stevens A. R. H., Cortese L., Padilla N. D., Davis T. A., Contreras S., Croton D., 2017, MNRAS, 464, 3850
Lee N. et al., 2013, ApJ, 778, 131
Leja J., Carnall A. C., Johnson B. D., Conroy C., Speagle J. S., 2019, ApJ, 876, 3
Liang L. et al., 2019, MNRAS, 489, 1397
Madau P., Dickinson M., 2014, ARA&A, 52, 415
Maraston C., Pforr J., Renzini A., Daddi E., Dickinson M., Cimatti A., Tonini C., 2010, MNRAS, 407, 830
Martis N. S., Marchesini D. M., Muzzin A., Stefanon M., Brammer G., da Cunha E., Sajina A., Labbe I., 2019, ApJ, 882, 65
Matthee J., Schaye J., 2019, MNRAS, 484, 915
McAlpine S. et al., 2016, Astron. Comput., 15, 72
McAlpine S. et al., 2019, MNRAS, 488, 2440
McLure R. J. et al., 2018a, MNRAS, 476, 3991
McLure R. J. et al., 2018b, MNRAS, 479, 25
Meurer G. R., Heckman T. M., Calzetti D., 1999, ApJ, 521, 64
Morrissey P. et al., 2007, ApJS, 173, 682
Muzzin A., van Dokkum P., Kriek M., Labbé I., Cury I., Marchesini D., Franx M., 2010, ApJ, 725, 742
Nersesian A. et al., 2019, A&A, 624, A80
Noeske K. G. et al., 2007, ApJ, 660, L43
Noll S., Burgarella D., Giovannoli E., Buat V., Marcillac D., Muñoz-Mateos J. C., 2009, A&A, 507, 1793
Oesch P. A. et al., 2010, ApJ, 725, L150
Oliver S. et al., 2010, MNRAS, 405, 2279
Pallero D., Gómez F. A., Padilla N. D., Torres-Flores S., Demarco R., Cerulo P., Olave-Rojas D., 2019, MNRAS, 488, 847
Pearson W. J. et al., 2018, A&A, 615, A146
Pforr J., Maraston C., Tonini C., 2012, MNRAS, 422, 3285
Pillepich A. et al., 2018, MNRAS, 473, 4077
Poglitsch A. et al., 2010, A&A, 518, L2
Popesso P. et al., 2019, MNRAS, 483, 3213
Price S. H., Kriek M., Feldmann R., Quataert E., Hopkins P. F., Faucher-Giguère C.-A., Kereš D., Barro G., 2017, ApJ, 844, L6
Renzini A., Peng Y.-j., 2015, ApJ, 801, L29
Rieke G. H. et al., 2004, ApJS, 154, 25
Rodighiero G. et al., 2010, A&A, 518, L25
Roebuck E., Sajina A., Hayward C. C., Pope A., Kirkpatrick A., Hernquist L., Yan L., 2016, ApJ, 833, 60
Rosas-Guevara Y., Bower R. G., Schaye J., McAlpine S., Dalla Vecchia C., Frenk C. S., Schaller M., Theuns T., 2016, MNRAS, 462, 190
Saftly W., Camps P., Baes M., Gordon K. D., Vand ewoude S., Rahimi A., Stalevski M., 2013, A&A, 554, A10
Salim S. et al., 2007, ApJS, 173, 267
Salmon B. et al., 2015, ApJ, 799, 183
Salpeter E. E., 1955, ApJ, 121, 161
Sánchez S. F. et al., 2018, Rev. Mex. Astron. Astrofis., 54, 217
Santini P. et al., 2009, A&A, 504, 751
Santini P. et al., 2012, A&A, 538, A33
Santini P. et al., 2017, ApJ, 847, 76

Schaye J. et al., 2015, MNRAS, 446, 521
Schaye J., Dalla Vecchia C., 2008, MNRAS, 383, 1210
Schreiber C. et al., 2015, A&A, 575, A74
Sklias P. et al., 2014, A&A, 561, A149
Smit R., Bouwens R. J., Franx M., Illingworth G. D., Labbé I., Oesch P. A., van Dokkum P. G., 2012, ApJ, 756, 14
Snyder G. F., Cox T. J., Hayward C. C., Hernquist L., Jonsson P., 2011, ApJ, 741, 77
Sobral D., Best P. N., Smail I., Geach J. E., Cirasuolo M., Garn T., Dalton G. B., 2011, MNRAS, 411, 675
Sparre M. et al., 2015, MNRAS, 447, 3548
Speagle J. S., Steinhardt C. L., Capak P. L., Silverman J. D., 2014, ApJS, 214, 15
Springel V., Di Matteo T., Hernquist L., 2005, MNRAS, 361, 776
Steinhardt C. L. et al., 2014, ApJ, 791, L25
Tacchella S., Trenti M., Carollo C. M., 2013, ApJ, 768, L37
Tescari E., Katsianis A., Wyithe J. S. B., Dolag K., Tornatore L., Barai P., Viel M., Borgani S., 2014, MNRAS, 438, 3490
Tomczak A. R. et al., 2016, ApJ, 817, 118
Torrey P. et al., 2015, MNRAS, 447, 2753
Utomo D., Kriek M., Labbé I., Conroy C., Fumagalli M., 2014, ApJ, 783, L30
Verley S., Corbelli E., Giovanardi C., Hunt L. K., 2010, A&A, 510, A64
Viaene S. et al., 2017, A&A, 599, A64
Vogelsberger M. et al., 2014, MNRAS, 444, 1518
Whitaker K. E., van Dokkum P. G., Brammer G., Franx M., 2012, ApJ, 754, L29
Whitaker K. E. et al., 2014, ApJ, 795, 104
Wiersma R. P. C., Schaye J., Theuns T., Dalla Vecchia C., Tornatore L., 2009, MNRAS, 399, 574
Wright E. L. et al., 2010, AJ, 140, 1868
Wuyts S., Labbé I., Förster Schreiber N. M., Franx M., Rudnick G., Brammer G. B., van Dokkum P. G., 2008, ApJ, 682, 985
Wuyts S., Franx M., Cox T. J., Hernquist L., Hopkins P. F., Robertson B. E., van Dokkum P. G., 2009, ApJ, 696, 348
Zubko V., Dwek E., Arendt R. G., 2004, ApJS, 152, 211

APPENDIX A: COMPARISON BETWEEN INTRINSIC AND INFERRED SFRS AND STELLAR MASSES

In this appendix, we compare the $SFR_{SED-FAST}$, $SFR_{24\,\mu m-Wuyts\,et\,al.\,2008}$, $SFR_{24,70,160\,\mu m-r\,Dale\&Helou\,2002}$, $SFR_{250,350,500\,\mu m-c\,Dale\&Helou\,2014}$, $SFR_{UV+IRX-\beta}$, and $M_{SED-FAST}$ calculated from the mock EAGLE + SKIRT galaxies as described in Section 3 to the intrinsic SFR_{Intr} and $M_{\star,\,Intr}$ provided in the EAGLE data base. In the top panels of Fig. A1 and Table A1, we present the offset in dex between the $M_{\star,\,SED-FAST}$ retrieved from the FAST SED fitting code (Kriek et al. 2009) and the intrinsic stellar masses $M_{\star,\,Intr}$. We show that at $z \simeq 4$ (the top left-hand panel of Fig. A1) the offset between the $M_{\star,\,SED-FAST}$ and $M_{\star,\,Intr}$ is $-0.1-0.1$ dex in the $\log_{10}(M_\star/M_\odot) = 8.5-10$ range. The $M_{\star,\,SED-FAST}/M_{\star,\,intr}$ ratio reaches -0.3 at $\log_{10}(M_\star/M_\odot) = 10.5$ at $z \simeq 4$ (the top left-hand panel of Fig. A1). In the middle panel of Fig. A1, we demonstrate that the offset is -0.1 to -0.01 dex in the $\log_{10}(M_\star/M_\odot) = 8.5-10.0$ range, while the $M_{\star,\,SED-FAST}$ are underestimated with respect to the $M_{\star,\,intr}$ by 0.17 dex at $\log_{10}(M_\star/M_\odot) = 10.5$ at $z \simeq 1$. Similarly, in the right-hand panel of Fig. A1 we show that the offset is -0.15 in the $\log_{10}(M_\star/M_\odot) = 8.5-10.0$ range. The derived stellar masses are underestimated by 0.25 dex at $\log_{10}(M_\star/M_\odot) = 10.5$. In conclusion, the stellar masses derived by FAST assuming an exponentially declining SFH [$SFR = exp(-t/\tau)$], the (Chabrier 2003) IMF, the Calzetti et al. (2000) dust attenuation law, and a

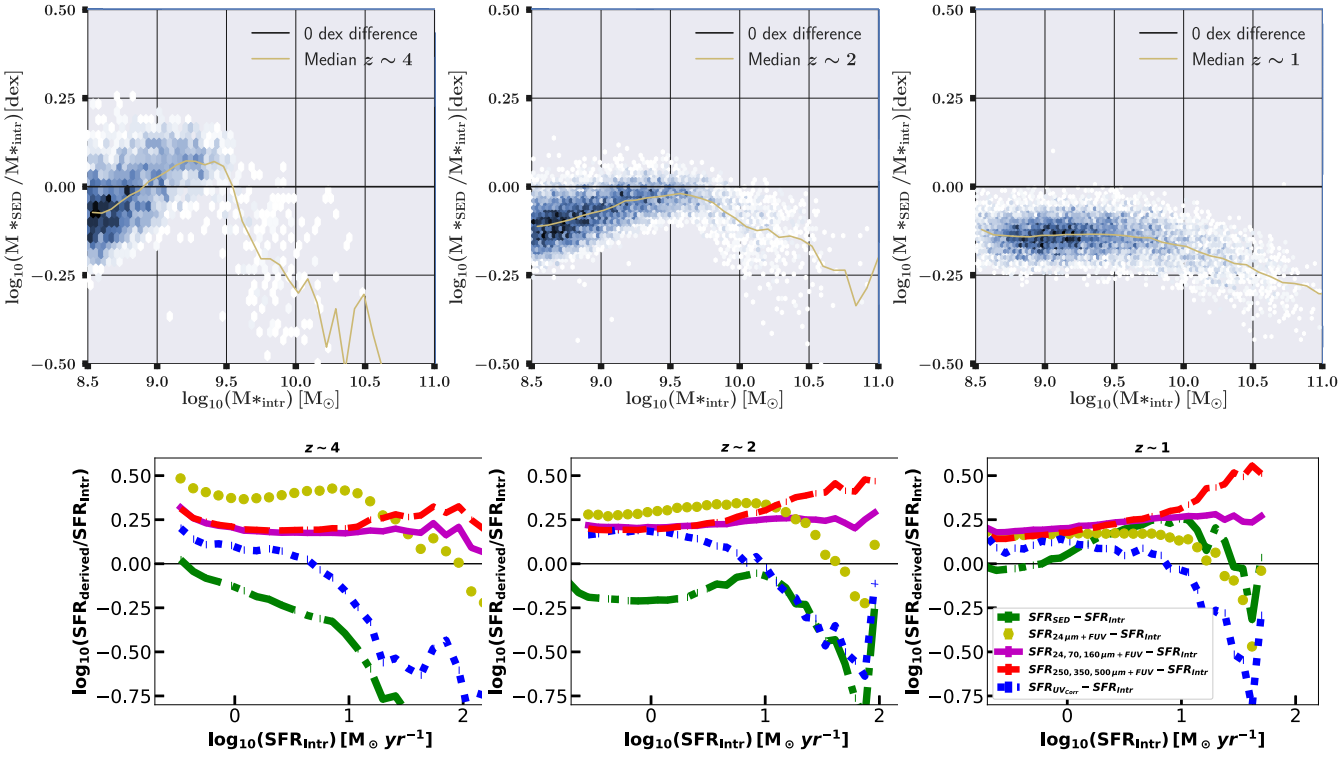

Figure A1. Top panels: Offset in dex between $M_{\star,\,SED-FAST}$, and $M_{\star,\,Intr}$. Bottom panels: offset between the $SFR_{24,70,160\,\mu m-r\,Dale\&Helou\,2002}$, $SFR_{SED-FAST}$, $SFR_{24\,\mu m-Wuyts\,et\,al.\,2008}$, $SFR_{UV+IRX-\beta}$, and SFR_{Intr}.

metallicity Z $= 0.2\ Z_{\odot}$ are typically underestimated with respect the intrinsic values by 0.1−0.3 dex at $z \simeq 1$–4.[10]

In the bottom panels of Fig. A1 and Table A2 (the left-hand panel $z \simeq 4$, middle panel $z \simeq 2$, and the right-hand panel $z \simeq 1$), we investigate the offset between the SFRs inferred from the indicators presented in Section 3 and the intrinsic SFRs (SFR_{intr}). The blue-dotted lines represent the offset between the $SFR_{UV+IRX-\beta}$ and intrinsic SFRs. At the lower SFR regime, the $SFR_{UV+IRX-\beta}$ are overestimated by $\simeq$0.1–0.2 dex. The authors suggested that the low-SFR objects are passive galaxies with a low dust content, where the UV radiation emitted by the evolved star population is interpreted as the formation of new stars by the UV indicator. On the other hand, the derived SFRs are underestimated by up to −0.65 dex for high-SFR objects. All the above are in agreement with the findings of Camps et al. (2016) for $z \simeq 0$. The UV-upturn (overestimation at low SFRs and underestimation at high SFRs) described above is evident as well in observations (Brown et al. 2003). The underestimation of the UV SFR with respect to other indicators in the high-SFR regime is also demonstrated in Katsianis et al. (2017a,b).

The dark green dot–dashed line represents the offset between $SFR_{SED-FAST}$ and SFR_{intr}. We demonstrate that the $SFR_{SED-FAST}$ are underpedicted at $z \simeq 4$ and $z \simeq 2$. The offset increases at high SFRs and can be up to −0.6 dex. This is in agreement with the findings of Conroy (2013) who demonstrated that SED-based values, assuming a range of SFHs (including exponentially declining), metallicities, and dust attenuation laws, tend to be underpredicted, compared to a mixed UV + IR indicator. A range of other studies (Brinchmann et al. 2004; Salim et al. 2007) suggested as well that SFRs based on modelling UV–optical SEDs carry systematic uncertainties and underpredict the values with respect to UV + TIR indicators. We find that SFR_{SED} are underestimated with respect the intrinsic values at $z \simeq 2$−4 but at $z \simeq 1$ the derived SFR_{SED} are overestimated, especially for higher intrinsic SFRs.

The yellow dot–dashed lines represent the offset between $SFR_{24\,\mu m-Wuyts\,et\,al.\,2008}$ and SFR_{intr}. For objects with intrinsic SFRs at the −0.5 to 1.0 regime SFRs are typically overestimated by 0.2–0.5 dex. This is in agreement with Rodighiero et al. (2010), De Looze et al. (2014), and Martis et al. (2019). In contrast, the derived $SFR_{24\,\mu m}$ are underestimated for higher star-forming objects. We note that the model assumed in the SKIRT post-process involves isotropically emitting star-forming regions that may not represent the variations of the radiation field in these regions sufficiently. As a result, some fraction of the diffuse dust in the EAGLE galaxies may not be sufficiently heated, producing a lower 24 μm flux than expected (Camps et al. 2016). In addition, the 24 μm inferred SFRs could be underpredicted from the simulations if a significant fraction of photons from young stars is not successfully absorbed by dust (Hayward et al. 2014; Sklias et al. 2014)

The magenta solid line/the red-dashed line represents the offset between $SFR_{24,70,160\,\mu m-r\,Dale\&Helou\,2002}/SFR_{250,350,500\,\mu m-c\,Dale\&Helou\,2014}$ and SFR_{intr}. The methods overpredict SFRs by $\simeq$ 0.1–0.5 dex at $z \simeq 4$, while at $z \simeq 2$ and $z \simeq 1$ the offset increases and is between $\simeq$ 0.2 and $\simeq$ 0.5 dex. This may be due to the fact that the emission from diffuse dust residing in the outskirts of the EAGLE + SKIRT galaxies is interpreted by the TIR indicator as a sign of star formation (Camps et al. 2016), while the dust is heated by an evolved star population and not by newly born stars. The above IR contamination is also found in observations (Helou et al. 2000; Bendo et al. 2015).

[10]Camps et al. (2016) also demonstrated that masses inferred from the *i*-band luminosity L_i and the $g-i$ colour (Cortese et al. 2012) from the EAGLE + SKIRT SEDs underestimate the stellar mass with respect to the intrinsic values by $\simeq$ 0.25 dex at $z \simeq 0$, pointing out differences between intrinsic and derived stellar masses.

Table A1. The offset in dex between the inferred and intrinsic stellar masses at a fixed intrinsic stellar mass.

Methodology	8.5	9.0	9.5	10.0	10.5	11.0
			Offset	(dex)		
$M_{\star,\,SED-FAST},\ z = 4$	−0.07	0.03	0.0	−0.26	−0.30	–
$M_{\star,\,SED-FAST},\ z = 2$	−0.11	− 0.06	− 0.02	−0.09	−0.17	−0.20
$M_{\star,\,SED-FAST},\ z = 1$	−0.12	− 0.14	− 0.14	−0.16	−0.24	−0.30

Table A2. The offset in dex between the inferred and intrinsic SFRs at a fixed intrinsic SFR.

Methodology	−0.5	0	0.5	1.0	1.5
			Offset	(dex)	
$SFR_{SED-FAST}, z = 4$	0.02	− 0.15	− 0.26	− 0.48	− 0.85
$SFR_{SED-FAST}, z = 2$	− 0.20	− 0.21	− 0.16	− 0.07	− 0.44
$SFR_{SED-FAST}, z = 1$	− 0.03	0.06	0.19	0.24	0.11
$SFR_{24\,\mu m-Wuyts\,et\,al.\,2008}, z = 4$	0.49	0.37	0.40	0.40	0.16
$SFR_{24\,\mu m-Wuyts\,et\,al.\,2008}, z = 2$	0.27	0.30	0.33	0.34	0.10
$SFR_{24\,\mu m-Wuyts\,et\,al.\,2008}, z = 1$	0.15	0.17	0.17	0.13	− 0.14
$SFR_{24,70,160\,\mu m-r\,Dale\&Helou\,2002}, z = 4$	0.32	0.22	0.20	0.19	0.19
$SFR_{24,70,160\,\mu m-r\,Dale\&Helou\,2002}, z = 2$	0.21	0.20	0.22	0.25	0.24
$SFR_{24,70,160\,\mu m-r\,Dale\&Helou\,2002}, z = 1$	0.18	0.21	0.24	0.27	0.25
$SFR_{250,350,500\,\mu m-c\,Dale\&Helou\,2014}, z = 4$	0.32	0.20	0.20	0.21	0.27
$SFR_{250,350,500\,\mu m-c\,Dale\&Helou\,2014}, z = 2$	0.20	0.20	0.23	0.30	0.40
$SFR_{250,350,500\,\mu m-c\,Dale\&Helou\,2014}, z = 1$	0.15	0.18	0.24	0.36	0.50
$SFR_{UV+IRX-\beta}, z = 4$	0.20	0.07	0.04	− 0.16	− 0.59
$SFR_{UV+IRX-\beta}, z = 2$	0.17	0.18	0.12	− 0.02	− 0.46
$SFR_{UV+IRX-\beta}, z = 1$	0.09	0.12	0.05	− 0.05	− 0.53

This paper has been typeset from a TEX/LATEX file prepared by the author.